X-ray analysis of praseodymia

Dissertation (kumulativ)

zur Erlangung des Grades eines
Doktors der Naturwissenschaften (Dr. rer. nat.)

dem Fachbereich Physik der Universität Osnabrück
vorgelegt von

Thomas Weisemöller, M. Sc.

Osnabrück, im Juli 2009

Contents

1 Introduction 1

2 Theoretical background 3

2.1 X-rays and their sources . . . 3
2.2 X-ray reflectivity . . . 6
2.2.1 Reflection at a surface . . . 8
2.2.2 Reflection at multiple interfaces . . . 9
2.2.3 Influence of interface roughness . . . 12
2.3 X-ray diffraction . . . 15
2.3.1 Kinematic diffraction theory . . . 16
2.3.2 Scattering at a single electron . . . 16
2.3.3 Scattering at a single atom . . . 17
2.3.4 Scattering at a single unit cell . . . 17
2.3.5 Diffraction at a finite single crystalline structure . . . 18
2.3.6 Diffraction at an infinite crystal . . . 18
2.3.7 Diffraction at a semi-infinite crystal . . . 20
2.3.8 Diffraction at a thin film . . . 22
2.3.9 Diffraction at a crystalline system . . . 23
2.3.10 Debye-Waller factor . . . 25
2.4 X-ray photoelectron spectroscopy . . . 26
2.5 Investigated materials . . . 27
2.5.1 Silicon(111) . . . 27
2.5.2 Praseodymium oxide . . . 28
2.5.3 Praseodymium oxide on silicon(111) . . . 29

3 Experimental setup 33

3.1 Sample preparation of praseodymium oxide on Si(111) . . . 33
3.2 Setup at HASYLAB . . . 35
3.2.1 Setup at beamline W1 . . . 35
3.2.2 Setup at beamline BW2 . . . 37
3.3 RodsNPlots - an X-ray diffraction analysis tool . . . 37
3.4 iXRR - an X-ray reflectivity analysis tool . . . 39

4 Epitaxy of Single Crystalline PrO_2 films on Si(111) *PREPRINT* **41**
T. Weisemoeller, C. Deiter, F. Bertram, S. Gevers, A. Giussani, P. Zaumseil, T. Schroeder, J. Wollschläger
Applied Physics Letters ***93****, 032905 (2008)*

5 Post deposition annealing induced transition from hexagonal Pr_2O_3 to cubic PrO_2 films on Si(111) *PREPRINT* **43**
T. Weisemoeller, F. Bertram, S. Gevers, A. Greuling, C. Deiter, H. Tobergte, M. Neumann, A. Giussani, T. Schroeder, J. Wollschläger
Journal of Applied Physics **105***, 124108 (2009)*

6 Effect of amorphous interface layers on crystalline thin film X-ray diffraction *PREPRINT* **45**
T. Weisemoeller, F. Bertram, S. Gevers, C. Deiter, A. Greuling, J. Wollschläger
Physical Review B ***79****, 245422 (2009)*

7 Further results on thin praseodymia films on Si(111) 47
7.1 Simulations of oxygen vacancies with RodsNPlots 47
7.2 On thin praseodymia films 50
    7.2.1 Multi column models and thin films 50
    7.2.2 Hydroxides 52
    7.2.3 On the Pr_2O_3 region 52
    7.2.4 On the PrO_2 region 54

8 Summary and Outlook 57

A List of peer-reviewed publications 59

Bibliography 61

List of Figures 66

B Acknowledgment 71

1 Introduction

Rare earth oxides have been studied intensively in the context of electro-optics [1], sensor technology [2] and catalytic reactions [3].

Furthermore, ultra thin rare earth oxide films attract increasing research interest as buffers for the integration of alternative semiconductors on the mature and technologically dominating Si wafer platform [4]. Here, one of the most promising future applications is the combination of Si wafers with materials like Ge (GOI) or GaAs, which are superior to Si with respect to some of their electronic properties. For example, GaAs features a higher electron mobility than Si, whereas Si features a higher hole mobility. Si on insulator (SOI) CMOS technologies already have an enormous commercial impact with Si dioxide as insulating material [5]. Alternative insulating materials are of course of high interest to enable the integration of different semiconductors and accordingly system on chip (SoC) solutions that cannot be built on Si alone. One of those alternatives is praseodymium oxide, which, in contrast to Si dioxide, grows single crystalline (with good lateral lattice matching) on Si(111) and features good insulating properties as well as a high dielectric constant.

In general, rare earth oxide films form interfacial silicate layers on Si when annealed to several hundred degree Celsius [6]. In this case, the interfacial reactivity is most pronounced for praseodymium among all lanthanides due to its large ion radius. Praseodymium oxide on Si is therefore a system that is obviously important for basic research of rare earth oxide on Si systems.

After an introduction to the theoretical background in chapter 2 and to the experimental setup in chapter 3, chapter 4 describes the successful preparation and investigation of single crystalline praseodymium dioxide on Si(111) (*Original publication Applied Physics Letters 93, 032905 (2008)*). The following chapter describes the transformation of hexagonal Pr_2O_3 to B-oriented PrO_2 with fluorite structure in more detail (*Original publication Journal of Applied Physics 105, 124108 (2009)*). Here, results from additional samples post deposition annealed at different temperatures are compared and investigated via X-ray reflectivity, X-ray diffraction and X-ray photoelectron spectroscopy. Also, the obtained results are compared to results for powder praseodymia.

Chapter 6 presents a new analysis method for X-ray diffraction data of crystalline structures with amorphous interface layers (*Original publication Physical Review B 79, 245422 (2009)*). This method was developed in the context of the above results for the praseodymium oxide on Si(111) system, but is transferable to many different material systems.

In addition to this, chapter 7 shows results of this thesis that have not been published in peer-reviewed journals currently. This includes simulated data for periodically ordered oxygen vacancies in praseodymium oxide as they were observed in the chapters above, as well as in-depth analysis of powder praseodymium oxide data. This analysis also takes into account the results of the previous chapters and discusses the resulting differences between powder praseodymia and thin films.

Finally, the most important results are summarized in chapter 8.

2 Theoretical background

X-rays are electromagnetic waves with photon energies ranging from about 100 eV to 100 keV. This range corresponds to wavelengths of about 100 Å to 0.1 Å, which is between ultraviolett and gamma rays. This chapter will explain physical properties of X-rays as well as their use for material science, in particular in the form of X-ray reflectivity (XRR) and X-ray diffraction (XRD) techniques. It will also give a short introduction to X-ray photoelectron spectroscopy (XPS) and to the material system of praseodymium oxide on Si(111).

2.1 X-rays and their sources

X-rays were discovered and systematically studied first by W.C. Röntgen in 1895 and have been of interest and of great practical use in material science and physics from that time on. In 1912, Max von Laue observed the first X-ray diffraction pattern from a crystal. One year later, Bragg established the new science of X-ray analysis of crystal structures. In the following decades, the standard X-ray tube, developed by W.D. Coolidge from General Electric Research Laboratories in New York, was used to generate X-rays (cf. Fig 2.1). Electrons were emitted from a glowing filament and accelerated towards a water cooled metal anode. The electrons were then decelerated in the anode, emitting a continuous radiation in the X-ray wave spectrum. This *bremsstrahlung* is superimposed by a sharper line spectrum. This sharper line spectrum is due to electron collisions which cause electrons to be removed

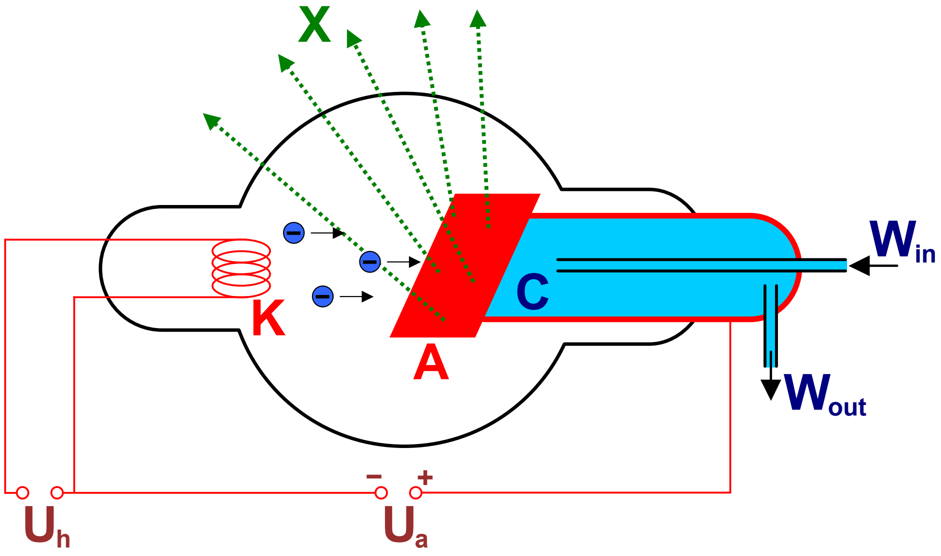

Figure 2.1: Coolidge tube, image taken from [7]. Voltage U_h is applied to the filament, which is in consequence heated so that electrons are emitted. These are accelerated by voltage U_a and decelerated when they hit the anode A. Due to this deceleration, X-rays X are emitted. The anode is cooled by the water cooler C with water connections W_{out} and W_{in}.

from one of the inner shells. Electrons from outer shells fill the holes created in this way and the excess potential energy is released as X-radiation. The energy of one of these photons is therefore identical to the difference of the potential energies of the two involved shells and thus depends on the anode material and on the involved shells (cf. Fig 2.2). This characteristic part of the radiation is emitted in addition to the *bremsstrahlung*, as noted above.

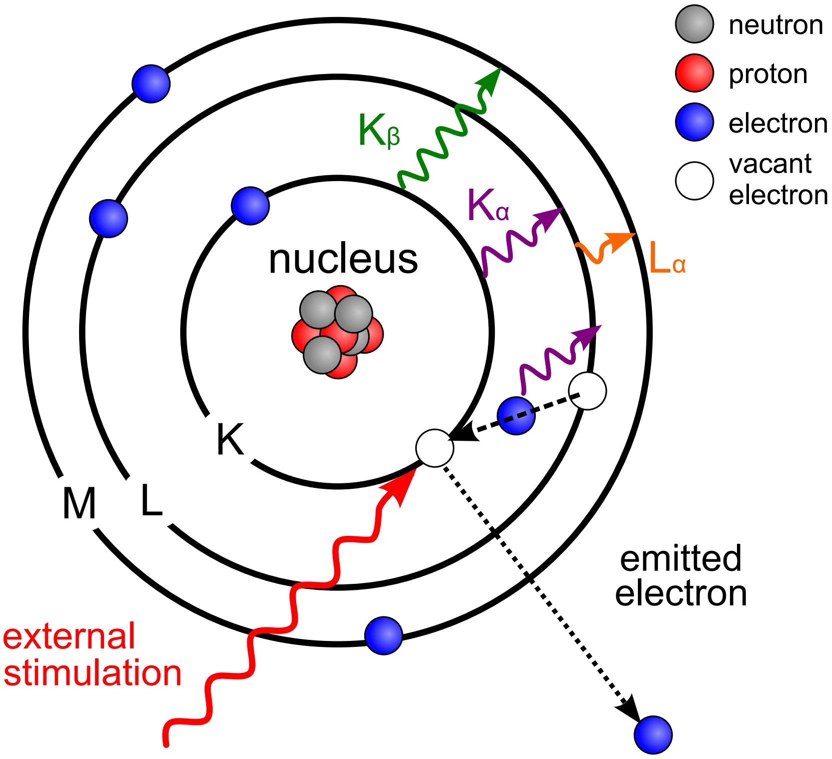

Figure 2.2: Atom model for X-ray emission in a tube, image taken from [8] and modified. External stimulation causes electrons to be emitted, the resulting electron holes are filled by electrons from higher shells. Excess energy is emitted in the form of X-radiation and contributes the characteristic part of the radiation.

Common copper anodes, for instance, have a strong K_α line, which is emitted when holes of the K-shell are filled with electrons from the L-shell. If the filling electrons originate from the next higher shell, the emitted radiation is defined as K_β and so forth.

Not until the 1960s, this concept was commercially enhanced by the introduction of *rotating anode generators*. The principle of these X-ray generators was identical to the Coolidge tubes, but the traditional fixed anode was replaced by a rotating anode. This technique provided better heat dissipation and thus higher total power. The brilliance of the X-ray beam increased. However, these proceedings were dwarfed by the emergence of synchrotron radiation sources in the 1970s and their successors, as shown in Fig 2.3.

Synchrotrons are cyclic particle accelerators. Electric and magnetic fields in a synchrotron are synchronized with the particle beam, which travels with relativistic speed in ultra high vacuum (UHV). In 2nd generation synchrotrons, like DORIS, where measurements discussed in this work were performed, the particle beam does not travel along a circular path, but along a polygon, which contains straight line segments. In some synchrotrons, these segments are very short and usually contain a wiggler or an undulator, that means a periodic series of magnets to deflect the particle beam as shown in Fig 2.4. In other synchrotrons, e.g. DORIS

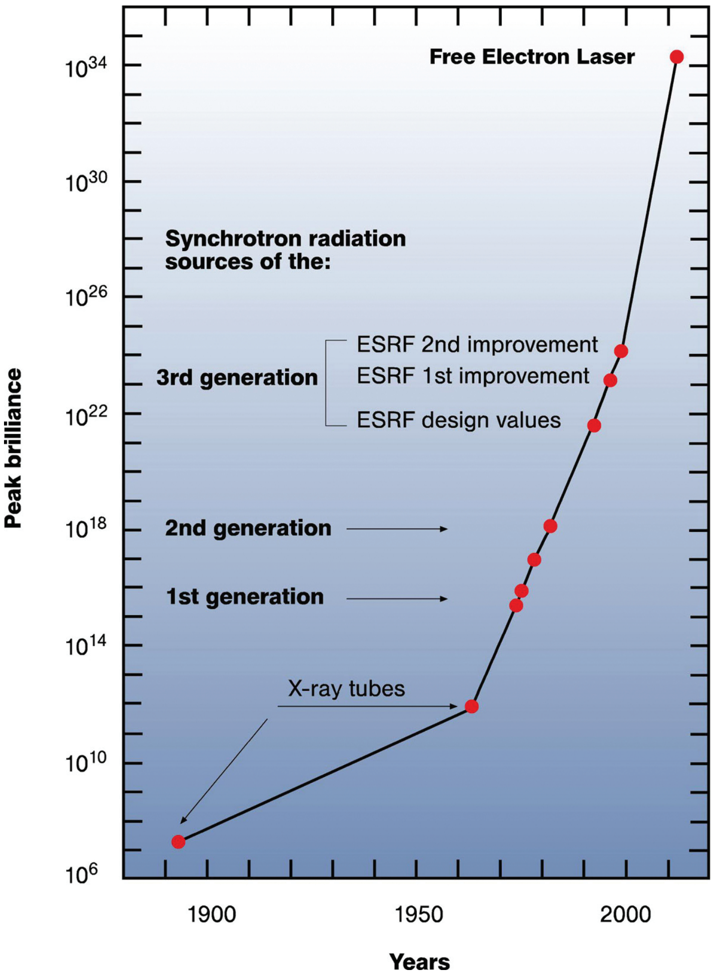

Figure 2.3: Brilliance with time, image taken from [9]. The development of synchrotron radiation sources enhanced the peak brilliance of X-ray sources dramatically. Free electron lasers provided further improvement recently.

III, several of these straight line segments are considerably longer, although this is of course not principally needed to produce and use synchrotron radiation. The emitted radiation due to the acceleration of the particles perpendicular to their direction of propagation is of much higher brilliance than the radiation of X-ray tubes.

Due to the still enormous progression in X-ray sources, experiments that were impossible only 10 or 20 years ago are now available for a broad community of scientists. Consequently, improvements in beam quality come along with new measuring techniques and new methods of data analysis. Because X-ray crystallography with high quality synchrotron radiation is such a new research field, enormous progress has been achieved recently and has to be expected for the near future. In this thesis, progress that has been achieved in our workgroup will be presented. This includes analysis methods suitable for the concrete praseodymia on Si(111) system as well as new analysis methods which are suitable for a wide range of material systems.

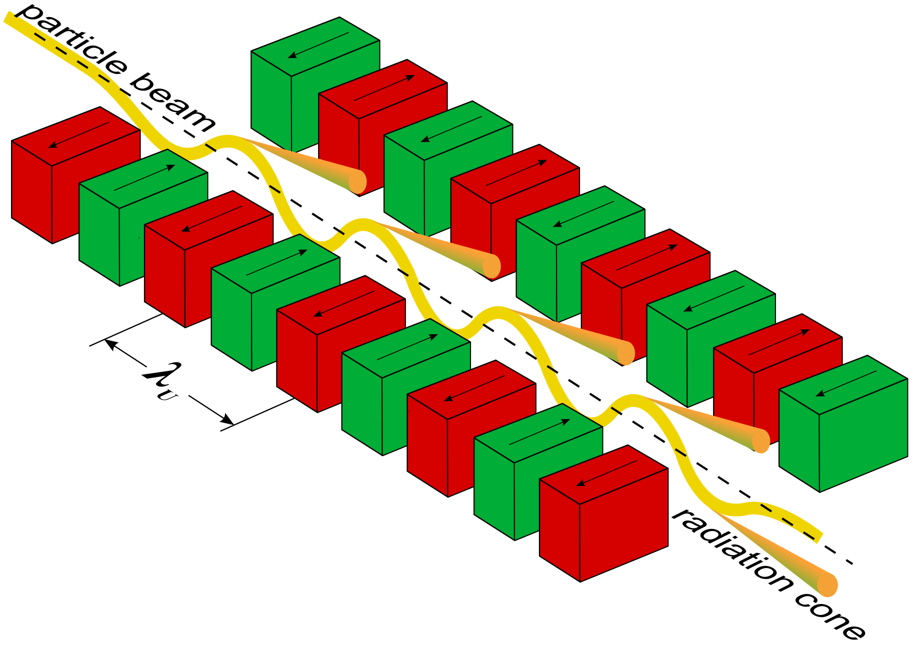

Figure 2.4: Sketch of an undulator/wiggler, image taken from [10]. Periodically ordered dipole magnets force the traversing particle beam to oscillate and radiate.

2.2 X-ray reflectivity

X-ray reflectivity (XRR) is a surface sensitive technique used for characterization of thin film and multilayer structures. When an electromagnetic wave hits a surface, it is (at least) partly reflected. The reflectivity depends on the wavelength dependent indices of refraction of the involved materials and the incident angle. In XRR, X-rays hit the target under small angles (cf. Fig. 2.5) and the intensities of the reflected beam are detected. The resulting intensity distribution gives information about the indices of refraction of different layers of a sample, the thickness of these layers, and about interface roughnesses.

An electromagnetic wave given by the electric field vector $\boldsymbol{E}(\boldsymbol{r}) = \boldsymbol{E_0}(\boldsymbol{r}) exp(i\boldsymbol{k_i} \cdot \boldsymbol{r})$ propagates according to the Helmholtz equation

$$\Delta \boldsymbol{E}(\boldsymbol{r}) + k^2 n^2(\boldsymbol{r}) \boldsymbol{E}(\boldsymbol{r}) = 0 \; , \tag{2.1}$$

with the absolute value $k = 2\pi/\lambda$ of the wave vector $\boldsymbol{k}_i$ and the wavelength λ. Atoms can be assumed to act as harmonic oscillators with frequencies ω_j. For an arrangement of N atoms, the index of refraction is

$$n^2(\boldsymbol{r}) = 1 + N \frac{e^2}{\epsilon_0} m \sum_{j=1}^{N} \frac{f_j}{\omega_j^2 - \omega^2 - 2i\omega\eta_j} \; , \tag{2.2}$$

with the frequency of the incoming wave ω, electron charge e and mass m, damping factors η_j and the strengths of the forced oscillations of the electrons of an atom f_j. f_j are com-

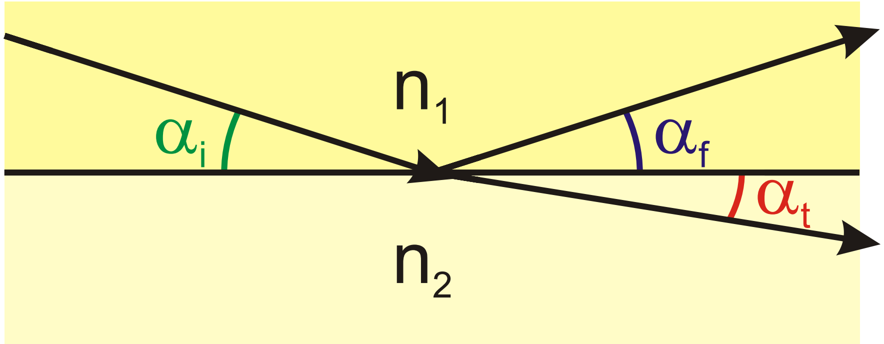

Figure 2.5: X-ray reflection and refraction at an interface. An X-ray beam hits the interface under an incidence angle α_i and is partly reflected under an angle $\alpha_f = \alpha_i$. The remaining part of the beam is refracted and transmitted under an angle α_t. In contrast to conventional optics, where angles are measured between direction of propagation and *surface normal*, the angles are measured between direction of propagation and *surface* in X-ray reflection.

plex numbers $f_j = f_j^0 + f_j'(E) + if_j''(E)$, which take into account dispersion and adsorption corrections. For X-rays ($\omega > \omega_j$), the index of refraction can also be described as

$$n(\boldsymbol{r}) = 1 - \delta(\boldsymbol{r}) + i\beta(\boldsymbol{r}) \ , \tag{2.3}$$

with dispersion

$$\delta(\boldsymbol{r}) = \frac{\lambda^2}{2\pi}\, r_e \rho(\boldsymbol{r}) \sum_{j=1}^{N} \frac{f_j^0 + f_j'(E)}{Z} \tag{2.4}$$

and absorption

$$\beta(\boldsymbol{r}) = \frac{\lambda^2}{2\pi}\, r_e \rho(\boldsymbol{r}) \sum_{j=1}^{N} \frac{f_j''(E)}{Z} = \frac{\lambda}{4\pi}\mu(\boldsymbol{r}) \ . \tag{2.5}$$

In Eqs. (2.4) and (2.5), the electron radius was introduced according to Thompson, with $r_e \approx 2,814 \cdot 10^{-5}$Å as well as the electron density $\rho(\boldsymbol{r})$, the number of electrons $Z = \sum_j Z_j$ with the number of electrons of each component of the material Z_j, and the absorption coefficient $\mu(\boldsymbol{r})$.

f_j^0 depends on the scattering vector $\boldsymbol{q} = \boldsymbol{k}_f - \boldsymbol{k}_i$, which is small because the incidence angle (and thus also the angle of the scattered wave) is also very small, as noted above. Therefore, q does not change significantly and f_j^0 can be approximated by $f_j^0 \approx Z_j$. Assuming a homogeneous medium and that energies of the the X-rays are far from absorption edges, the refractive index can be approximated by

$$n = 1 - \frac{\lambda^2}{2\pi} r_e \rho + i \frac{\lambda}{4\pi} \mu \tag{2.6}$$

$$= 1 - \delta + i\beta \ . \tag{2.7}$$

δ is 0 in vacuum and is usually between 10^{-6} and 10^{-4} for solid materials, β is typically one or two orders of magnitude smaller. The real part of the refractive index is accordingly slightly smaller than unity. It is noteworthy that this does *not* mean that the speed of light in solid materials c/n is higher than in vacuum, which would contradict fundamental physics. c/n is the *phase* velocity and *not* the *group* velocity, which is indeed smaller than c. Hence, X-rays in solid materials are no way to send information faster than c.

Because the refractive index of a medium is smaller than the one of vacuum, total reflection occurs if an X-ray wave hits a vacuum/medium interface under a sufficiently small angle. n_{air} can be approximated to unity as δ_{air} is very small due to the low density of air. Total reflection consequently also happens at air/medium interfaces, which are common for X-ray reflectivity measurements. The law of refraction gives $\cos\alpha_i = (1-\delta)\cos\alpha_t$. Total reflection occurs if the angle of the transmitted beam α_t is smaller than zero. For small angles, with $cos\ \alpha \ \approx 1 - \frac{\alpha^2}{2}$, this gives a critical angle of

$$\alpha_c \approx \sqrt{2\delta} \ , \tag{2.8}$$

which is typically below 1° for a vacuum(air)/medium interface.

2.2.1 Reflection at a surface

In the following, reflectivity of a vacuum/medium interface is calculated. Since $n_{air} \approx n_{vacuum} = 1$, these calculations are portable to an air/medium interface for solid state media. A schematic drawing of the involved media and angles is shown in Fig. 2.5.

A plane wave $\boldsymbol{E}_i(\boldsymbol{r}) = (0,\ A_i,\ 0)\ exp(i\ \boldsymbol{k}_i \cdot \boldsymbol{r})$ with the wave vector $\boldsymbol{k}_i = k\,(\cos\alpha_i,\ 0,\ -\sin\alpha_i)$ hits the interface between vacuum ($n = n_2 = 1$) and medium ($n = n_1$). The reflected and transmitted waves are accordingly $\boldsymbol{E}_r(\boldsymbol{r}) = (0,\ A_r,\ 0)\ exp(i\ \boldsymbol{k}_f \cdot \boldsymbol{r})$ and $\boldsymbol{E}_t(\boldsymbol{r}) = (0,\ A_t,\ 0)\ exp(i\ \boldsymbol{k}_t \cdot \boldsymbol{r})$ with $\boldsymbol{k}_f = k\,(\cos\alpha_i,\ 0,\ \sin\alpha_i)$, where the components $\boldsymbol{k}_t = (k_{t,x},\ 0,\ k_{t,z})$ result from the law of refraction.

In the case of s-polarization, the electric field vector is oriented perpendicular to the (x,z) scattering plane in y-direction. Because the tangential components of the electric and magnetic field must be continuous at the surface ($z = 0$), reflectivity coefficient $r_s = A_r/A_i$ and transmission coefficient $t_s = A_t/A_i$ are described by the Fresnel formulas

$$r_s = \frac{k_{i,z} - k_{t,z}}{k_{i,z} + k_{t,z}} \qquad \text{and} \tag{2.9}$$

$$t_s = \frac{2k_{i,z}}{k_{i,z} + k_{t,z}} \ . \tag{2.10}$$

With $k_{t,z} = nk\sin\alpha_t = k\sqrt{n^2 - \cos^2\alpha_i}$, the total intensity R of the reflected wave is $|r_s|^2$.

As noted above, n can be approximated by unity for X-rays. The results for p-polarized X-rays,

$$r_p = \frac{n^2 k_{i,z} - k_{t,z}}{n^2 k_{i,z} + k_{t,z}} \qquad \text{and} \tag{2.11}$$

$$t_p = \frac{2k_{i,z}}{n^2 k_{i,z} + k_{t,z}} \ , \tag{2.12}$$

are therefore in good approximation identical to the ones for s-polarized X-rays. Because of that, only the case of s-polarized X-rays will be considered in the following. A theoretically calculated example of the scattering angle resolved reflectivity at a single interface is shown in Fig. 2.6.

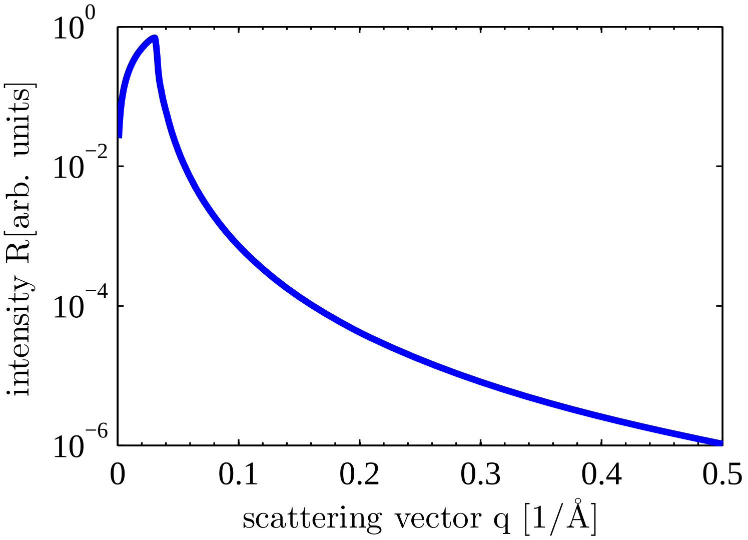

Figure 2.6: Simulated intensity of a wave reflected at a vacuum/Si interface. The photon energy is 10 keV and an intensity R of 1.0 means that the wave is totally reflected. The simulation includes a linear increase of the reflected intensity with small scattering vectors. This *footprint* is due to the assumed finite size of the sample and the three-dimensional extension of the beam.

2.2.2 Reflection at multiple interfaces

Real world systems usually consist of more than one interface. An N layer system is shown in Fig. 2.7, where layer $N+1$ is the substrate of infinite thickness.

A recursive approach to calculate the intensity of the reflected beam according to the model shown in Fig. 2.7 was established by Parratt [12] in 1954. The continuity of the tangential components of the electric field vector at an interface between layers $j-1$ and j can be

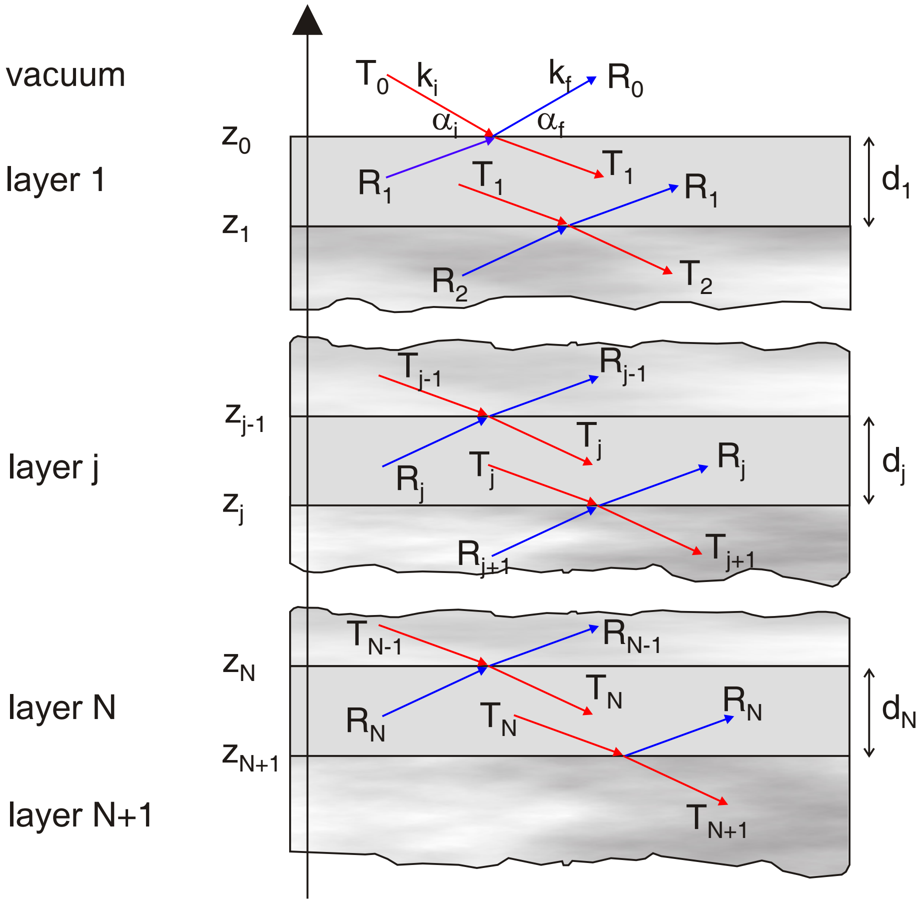
vacuum
layer 1
layer j
layer N
layer N+1
z0
z1
zj-1
zj
zN
zN+1
T0
ki
kf
R0
αi
αf
R1
T1
T1
R1
R2
T2
d1
Tj-1
Rj-1
Tj
Rj
Tj
Rj
Rj+1
Tj+1
dj
TN-1
RN-1
TN
RN
TN
RN
TN+1
dN

Figure 2.7: X-ray reflectivity at multiple interfaces, image taken from [11] and translated. A part of the previously transmitted beam T_{j-1} (red) is reflected at the interface at z_{j-1} as beam R_{j-1} (blue), the rest of the beam is transmitted as T_j. The distance between two interfaces is d_j. Multiple scattering effects are taken into account, so that a part of the reflected wave R_j is reflected again at the interface at z_{j-1}. Its amplitude is therefore added to T_j.

described as

$$a_{j-1}T_{j-1} + a_{j-1}^{-1}R_{j-1} = \qquad a_j^{-1}T_j + a_jR_j \tag{2.13}$$

$$\left(a_{j-1}T_{j-1} - a_{j-1}^{-1}R_{j-1}\right) f_{j-1}k_1 = \left(a_j^{-1}T_j - a_jR_j\right) f_jk_1 \ . \tag{2.14}$$

The amplitude factor a_n for the perpendicular layer thickness d_j is

$$a_j = \exp\left(-ik_1f_j\frac{d_j}{2}\right) \qquad \text{and} \tag{2.15}$$

$$f_jk_1 = k_{z,j} = k\sqrt{\left(n_j^2 - \cos^2\alpha_i\right)} \ . \tag{2.16}$$

This can also be written as recursive formula [12]

$$R_{j-1,j} = a_{j-1}^4 \frac{R_{j,j+1} + F_{j-1,j}}{1 + R_{j,j+1} F_{j-1,j}} \tag{2.17}$$

with

$$R_{j,j+1} = a_j^2 \left(R_j / T_j\right) \qquad \text{and} \tag{2.18}$$

$$F_{j-1,j} = \frac{f_{j-1} - f_j}{f_{j-1} + f_j} = \frac{k_{z,j+1} - k_{z,j}}{k_{z,j+1} + k_{z,j}}, \tag{2.19}$$

with the scattering vector $(k_i - k_f) = 2\,k_{z,j}$. Assuming an infinite thickness of the substrate, the recursive calculation of the reflected intensity starts with $R_{N,N+1} = 0$ (all intensity reflected at the lower substrate boundary is absorbed). The amplitude factor of the top vacuum/air layer is defined as $a_0 = 1$, so that the reflected *intensity* is

$$R = \frac{I_r}{I_0} = \left|\frac{R_0}{T_0}\right|^2 = \left|R_{0,1}\right|^2 \ . \tag{2.20}$$

According to [13], the amplitudes of reflected and transmitted wave in layer $j+1$ are

$$R_{j+1} = \frac{1}{t_{j+1,j}} \left\{T_j\ r_{j+1,j} \exp\left(-i\left(k_{z,j+1} + k_{z,j}\right) z_j\right) + R_j \exp\left(-i\left(k_{z,j+1} - k_{z,j}\right) z_j\right)\right\} \tag{2.21}$$

$$T_{j+1} = \frac{1}{t_{j+1,j}} \left\{T_j \exp\left(i\left(k_{z,j+1} - k_{z,j}\right) z_j\right) + R_j\ r_{j+1,j} \exp\left(i\left(k_{z,j+1} + k_{z,j}\right) z_j\right)\right\} \ . \tag{2.22}$$

The component of the scattering vector perpendicular to the surface in layer j is

$$q_{z,j} = 2\,k_{z,j} = \left(k_i - k_f\right)_z \ . \tag{2.23}$$

In the following, $q_{z,j}$ will be referred to as q_j because the scattering components parallel to the surface are zero in XRR. The Fresnel coefficient at the interface at z_j between layer j and layer $j+1$ is consequently

$$r_{j,j+1} = \frac{q_j - q_{j+1}}{q_j + q_{j+1}} \ . \tag{2.24}$$

As noted above, the substrate is assumed to be of infinite thickness. Therefore, no reflected beam R_{N+1} from the substrate bottom is assumed and the recursive calculation starts with

$$R_{N,N+1} = \frac{q_N - q_{N+1}}{q_N + q_{N+1}} = r_{N,N+1} \ . \tag{2.25}$$

Reflected amplitudes at the following interfaces are recursively calculated by

$$R_{j-1,j} = \frac{r_{j-1,j} + R_{j,j+1} \exp\left(i d_j q_j\right)}{1 + r_{j-1,j} R_{j,j+1} \exp\left(i d_j q_j\right)} \tag{2.26}$$

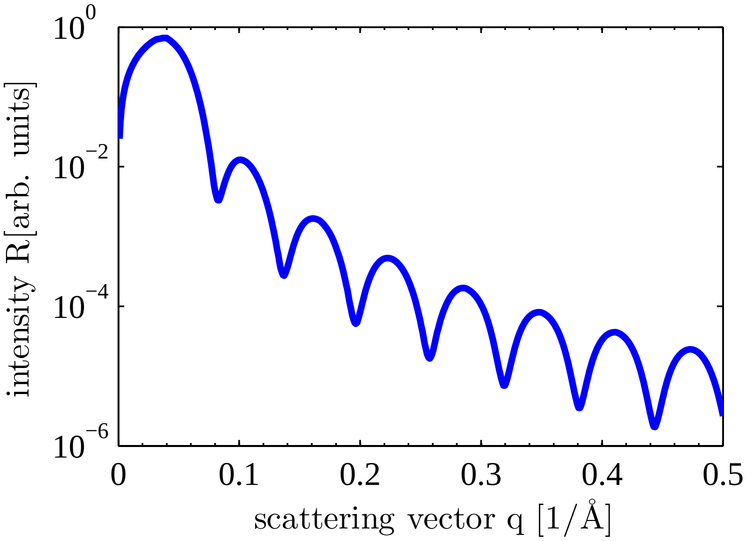

Figure 2.8: Simulated intensity of a wave reflected at a substrate with 10 nm praseodymium dioxide on top. The photon energy is 10 keV and an intensity R of 1.0 means that the wave is totally reflected. Interfaces are perfectly sharp (no roughness). The angle dependent oscillations are due to the oxide layer of finite thickness.

until the vacuum/medium interface is reached and the angle dependent normalized total reflected *intensity*

$$R = \frac{I_r}{I_0} = \left| \frac{R_0}{T_0} \right|^2 = |R_{0,1}|^2 \tag{2.27}$$

results.

The simulated intensity of a sample with Si substrate and 10 nm praseodymium dioxide layer on top is shown in Fig. 2.8. Intensity oscillations occur due to alternately appearing constructive and destructive interference. The Bragg condition using the example of X-ray reflectivity is shown in Fig. 2.9 for clarification. Intensity *maxima* appear for scattering vectors causing *constructive* interference, *minima* appear for scattering vectors causing *destructive* interference.

2.2.3 Influence of interface roughness

Until here, only perfectly sharp interfaces were considered. In practice, however, all interfaces and therefore also surfaces are rough. The assumption that the index of refraction changes abruptly from n_{j+1} to n_j is of course inaccurate. In principle, the distribution of the index is three-dimensional ($n(x, y, z)$). Because the scattering vector $\boldsymbol{q} = \boldsymbol{k}_f - \boldsymbol{k}_i$ in XRR measurements has neither x- nor y-component, it is sufficient to assume a one-dimensional distribution $n(z)$.

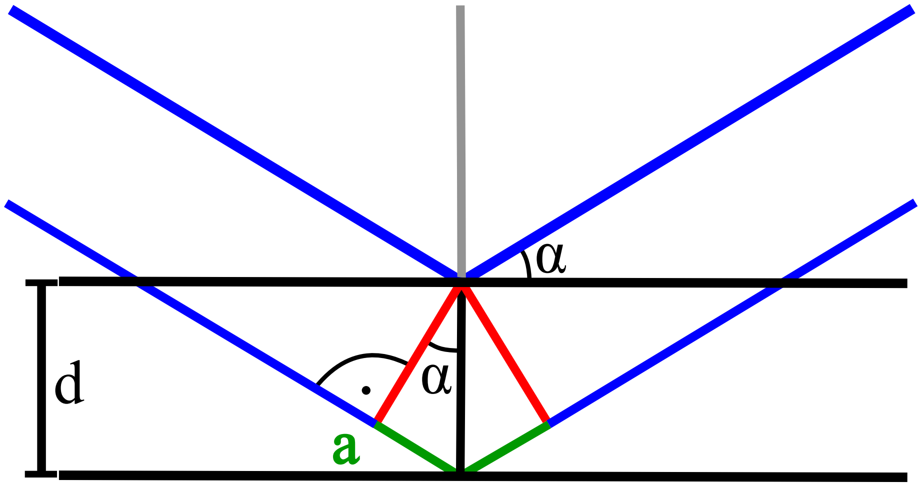

Figure 2.9: Bragg condition using the example of X-ray reflectivity, image taken from [14] and modified. The path difference (dark red) between the waves (blue) reflected at the under and upper layer (black) is $\delta = 2d\sin\Theta$ with the distance between the layers d and the incidence angle Θ. If this incidence angle dependent path difference is a multiple of the wavelength, constructive interference occurs.

In order to estimate the influence of roughened interfaces, one can replace the rough interface by an ensemble of sharp interfaces with z-coordinates $z_j + z$, which are weighted by a probability density $P(z)$, with mean value

$$\mu_j = \int z\, P(z) dz \ , \tag{2.28}$$

and with the root-mean-square (rms) roughness

$$\sigma_j^2 = \int (z - \mu_j)^2\, P_j(z) dz \ . \tag{2.29}$$

The function $f_j(k)$, which is the Fourier transform of $P_j(z)$ for real k values, is defined by

$$f_j(k) = \langle \exp\{-i\, k\,(z-\mu_j)\}\rangle_{P_j(z)} \tag{2.30}$$

$$= \exp(ik\mu_j) \int \exp(-ikz)\, P_j(z) dz \ . \tag{2.31}$$

With the averaged right-hand sides of Eqs. (2.21) und (2.22), one obtains

$$R_{j+1} = \frac{1}{\tilde{t}_{j+1,j}} \{T_j\ \tilde{r}_{j+1,j} \exp[-i(k_{z,j+1} + k_{z,j})\, z_j] + R_j \exp[-i(k_{z,j+1} - k_{z,j})\, z_j]\} \tag{2.32}$$

$$T_{j+1} = \frac{1}{f_t \tilde{t}_{j+1,j}} \{T_j \exp[i(k_{z,j+1} - k_{z,j})\, z_j] + R_j\ f_r \tilde{r}_{j+1,j} \exp[i(k_{z,j+1} + k_{z,j})\, z_j]\} \ . \tag{2.33}$$

with the modified Fresnel coefficients for rough interfaces

$$\tilde{r}_{j+1,j} = \frac{f_j\left(k_{z,j+1} + k_{z,j}\right)}{f_j\left(k_{z,j+1} - k_{z,j}\right)} r_{j+1,j} \qquad \text{and} \tag{2.34}$$

$$\tilde{t}_{j+1,j} = \frac{1}{f_j\left(k_{z,j+1} - k_{z,j}\right)} t_{j+1,j} \ . \tag{2.35}$$

For real arguments, $|f_r|$ and $|f_t|$ are unity. Although $k_{z,j}$ have noticeable imaginary parts in the region of the critical angle in general, this is not the case for X-rays [13]. Therefore, $|f_r|$ and $|f_t|$ can be set to unity in very good approximation for XRR.

Assuming a continuous refractive index profile

$$n_j(z) = \frac{n_j + n_{j+1}}{2} - \frac{n_j - n_{j+1}}{2} \mathrm{erf}\left(\frac{z - z_j}{\sqrt{2}\sigma_j}\right) \tag{2.36}$$

with the error function

$$\mathrm{erf}(z) = \frac{2}{\sqrt{\pi}} \int\limits_0^z \exp\left(-t^2\right) dt \ , \tag{2.37}$$

a Gaussian probability density

$$P_j(z) = \frac{1}{\sqrt{2\pi}\sigma_j} \exp\left(-\frac{z^2}{2\sigma_j^2}\right) \tag{2.38}$$

results. The corresponding Fresnel coefficients

$$\tilde{r}_{j+1,j} = r_{j,j+1} \exp\left(-2k_{z,j}k_{z,j+1}\sigma_j^2\right) \qquad \text{and} \tag{2.39}$$

$$\tilde{t}_{j+1,j} = t_{j,j+1} \exp\left(+\left(k_{z,j}k_{z,j+1}\right)^2 \sigma_j^2/2\right) . \tag{2.40}$$

describe reflectivity and transmittance of a single interface. Factor $\exp\left(-2k_{z,j}k_{z,j+1}\sigma_j^2\right)$ is also known as Nevot-Croce-Factor [15].

Equation (2.32) develops from an averaging *after* summing up the phase factors. If the calculation is done the other way round, the results differ slightly [16]:

$$\tilde{r}_{j+1,j} = r_{j,j+1} \exp\left(-2k_{z,j}^2\sigma_j^2\right) \qquad , \tag{2.41}$$

$$\tilde{t}_{j+1,j} = t_{j,j+1} \exp\left(-\left(k_{z,j} - k_{z,j+1}\right)^2 \sigma_j^2/2\right) \ . \tag{2.42}$$

Also, the index of refraction profile can be assumed to be in the form of hyperbolic tangent instead of the form of error function. This is usually done to simulate vapor/liquid boundaries. As such samples were not investigated in this work, the differences between these methods will not be discussed here in detail.

2.3 X-ray diffraction

In the field of X-ray diffraction (XRD), crystalline solid state materials are investigated. In general, diffraction occurs when waves encounter an obstacle. The resulting diffraction pattern gives information about the obstacle(s). In the case of XRD, the obstacles are electrons of the atoms in the solid. If the arrangement of the electrons is periodical, constructive interference occurs, whereas in cases of random electron arrangement, the diffracted intensity is white noise.

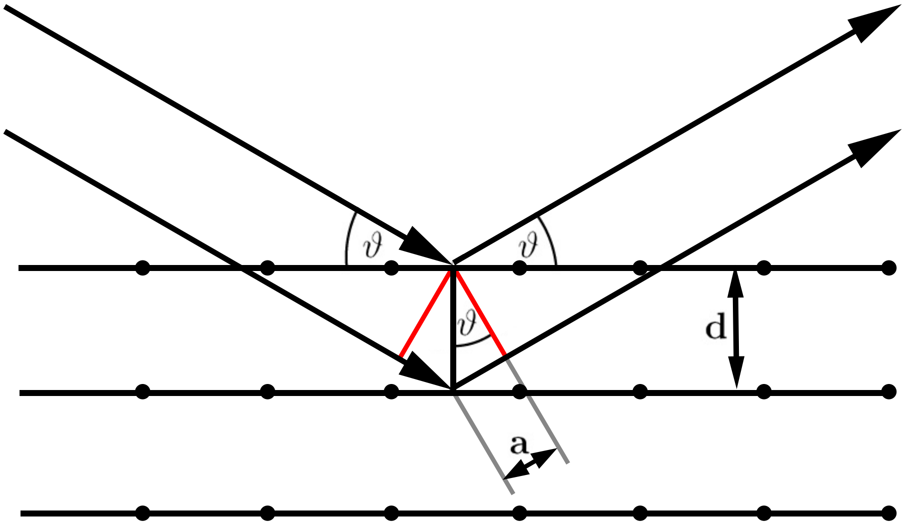

Figure 2.10: Bragg condition at atomic planes, image taken from [17]. Waves diffracted at periodically ordered layers with distance d have a path difference of $2a = 2d \sin\vartheta$. If this path difference is a multiple of the wavelength for neighboring layers, the same is also true for the path difference between any equidistant layers. The Bragg condition is fulfilled and waves diffracted at all these layers therefore interfere constructively for certain scattering vectors.

Periodical arrangements of electrons typically occur if the atoms which the electrons are bound to are ordered periodically. It is important to note that it is sufficient if this ordering is only partly. The waves diffracted at the ordered structures then fulfill the Bragg condition for certain scattering vectors. A simple example of such a structure is shown in Fig. 2.10. Depending on the orientation and size of the periodic structure, a characteristic diffraction pattern occurs.

To fulfill the Bragg condition $2\, d_{hkl} \sin\theta = n\, \lambda$ of the first order ($n = 1$), the wavelength must be smaller or equal to $2\, d_{hkl}$. This is the reason why only relatively hard X-rays with relatively small wavelengths can be used to investigate structures in the sub nanometer regime. If the wavelength is much smaller than the investigated structures, the incidence angle becomes extremely small. Typical photon energies to investigate single crystalline structures via XRD are therefore about 10 keV (1.24 Å wavelength). Higher energies of 20+ keV are in principle useful for studies which include higher order Bragg conditions, but the availability of high brilliance radiation sources is limited.

2.3.1 Kinematic diffraction theory

In order to analyze the naturally complex structures of real samples, simplifications are inevitable. The analysis in the following chapter is based on the common kinematic diffraction theory, which bases on three fundamental simplifications:

- Multiple scattering processes do not happen, so that each photon is diffracted only once.
- The intensity of the incidence beam is the same at all layers of a structure. In other words, absorption is neglected. This simplification is of course problematic for thick structures and small incidence angles, because the photons travel a relatively long way through the sample. It also implies that the photon energies do not correspond to absorption edges of the atoms of the sample. Hence, this principle is only applied with exception of the substrate.
- Refraction does not play a role for the intensity of the diffracted wave. This assumption is reasonable because the medium dependent changes of the index of refraction is rather small for X-rays (cf. chapter 2.2). However, this simplification requires that total reflection does not happen, so that small incidence angles and small angles of the diffracted beam are not measured.

Further details can be found in [18].

2.3.2 Scattering at a single electron

The amplitude A_0 of a wave scattered at a single electron at the location $\boldsymbol{r}_e$ is

$$A(\boldsymbol{q}) = A_0 \frac{e^2}{m_e c^2} \frac{1}{R_0}\, e^{i\, \boldsymbol{q} \cdot \boldsymbol{r}_e} \tag{2.43}$$

according to the Thompson formula. The scattering vector $\boldsymbol{q}$ is the difference of the wave vectors of the incoming and the scattered wave. The distance between the detector (which detects the scattered photons) and the electron R_0, elementary charge e, electron mass m_e and speed of light c are assumed to be constant and their influence is summed up in the constant C, so that scattering at an electron is described as

$$A(\boldsymbol{q}) = A_0\, C\, e^{i\, \boldsymbol{q} \cdot \boldsymbol{r}_e} \; . \tag{2.44}$$

2.3.3 Scattering at a single atom

Scattering at an atom is described by the phase correct summation of the waves diffracted at the electrons of the atom. The amplitude of the diffracted wave is therefore

$$A(\boldsymbol{q}) = A_0\, C \int d^3r \rho\,(\boldsymbol{r})\; e^{i\,\boldsymbol{q}\cdot\,(\boldsymbol{r}_a + \boldsymbol{r})} \tag{2.45}$$

with the atom position $\boldsymbol{r}_a$. The amplitude is smaller than just the amplitude for scattering at a single electron multiplied by the number of electrons, as the scattered waves do not interfere completely constructively. This can be described by the *atomic form factor*, which depends on the absolute scattering vector and can be approximated by quantum mechanical methods. In this work, atomic electron shells are assumed to be spherically symmetrical and are described by four gaussian functions

$$f(q) = \sum_{i=1}^{4} a_i\; e^{-b_i\left(\frac{q}{4\pi}\right)^2} + c\ . \tag{2.46}$$

The amount of constructive and destructive interference is consequently expressed by the atomic form factor $f(q)$ and the intensity of a wave scattered at an atom is

$$A(\boldsymbol{q}) = A_0\, C\, f(q)\, e^{i\,\boldsymbol{q}\cdot\boldsymbol{r}_a}\ . \tag{2.47}$$

2.3.4 Scattering at a single unit cell

Scattering at a unit cell is described simply by continuation of the principles used to describe scattering at an atom. A unit cell is consequently viewed as a number of (atomic) scattering centers that interfere constructively and destructively depending on their relative positions and the scattering vector. The amplitude of a wave scattered at a unit cell of N atoms is

$$A(\boldsymbol{q}) = A_0\, C \sum_{j=1}^{N} f_j\,(q)\; e^{i\,\boldsymbol{q}\cdot\,(\boldsymbol{r}_n + \boldsymbol{r}_j)} \tag{2.48}$$

$$= A_0\, CF\,(q)\; e^{i\,\boldsymbol{q}\cdot\boldsymbol{r}_n}\ , \tag{2.49}$$

with the structure factor

$$F\,(q) = \sum_{j=1}^{N} f_j\,(q)\; e^{i\,\boldsymbol{q}\cdot\boldsymbol{r}_j}\ . \tag{2.50}$$

The positions of the atoms $\boldsymbol{r}_n + \boldsymbol{r}_j$ are composed of the position of the unit cell $\boldsymbol{r}_n$ and the relative atom positions $\boldsymbol{r}_j$. It is important to note that scattering at a unit cell depends on the *vector* $\boldsymbol{q}$ and not just on the absolute value of the scattering vector q. This is because a unit cell is not assumed to be of spherical symmetry, in contrast to an atom, as noted above.

2.3.5 Diffraction at a finite single crystalline structure

Diffraction at a crystalline structure consisting of several unit cells is described by the phase correct summation of the amplitudes of the waves scattered at the involved unit cells, divided by the number of summands. The term *diffraction* is used for these phenomena in contrast to *scattering* in the previous chapters because the scattering centers have periodical ordering, so that the Bragg condition plays an important role.

The amplitude of the diffracted wave is

$$A\left(\boldsymbol{q}\right) = A_0\, C \sum F_n\left(\boldsymbol{q}\right)\, e^{i\boldsymbol{q}\cdot\boldsymbol{r}_n} \quad . \tag{2.51}$$

We choose to describe the periodic ordering of the unit cells as a three-dimensional string of unit cells along the unit cell vectors $\boldsymbol{a}$, $\boldsymbol{b}$ and $\boldsymbol{c}$, with N_1, N_2 and N_3 unit cells, respectively. The amplitude of a wave diffracted at this array of $N_1 \cdot N_2 \cdot N_3$ unit cells is hence

$$\begin{aligned} A\left(\mathbf{q}\right) &= A_0\, C\, \frac{1}{N_1 N_2 N_3} F\left(\boldsymbol{q}\right) \sum_{n_1=0}^{N_1-1} \sum_{n_2=0}^{N_2-1} \sum_{n_3=0}^{N_3-1} e^{i\boldsymbol{q}\cdot\, (n_1\boldsymbol{a} + n_2\boldsymbol{b} + n_3\boldsymbol{c})} && (2.52) \\ &= A_0\, C\, \frac{1}{N_1 N_2 N_3} F\left(\boldsymbol{q}\right) \sum_{n_1=0}^{N_1-1} e^{i\, n_1\, \boldsymbol{q}\cdot\boldsymbol{a}} \sum_{n_2=0}^{N_2-1} e^{i\, n_2\, \boldsymbol{q}\cdot\boldsymbol{b}} \sum_{n_3=0}^{N_3-1} e^{i\, n_3\, \boldsymbol{q}\cdot\boldsymbol{c}} \quad . && (2.53) \end{aligned}$$

The unit cell sums of one dimension correspond to geometric series each, so that

$$\begin{aligned} S_{0,N}\left(x\right) &= \sum_{n=0}^{N-1} e^{i\, n\, x} && (2.54) \\ &= \frac{1 - e^{i\, N\, x}}{1 - e^{i\, x}} \quad . && (2.55) \end{aligned}$$

With $x = \boldsymbol{q}\cdot\boldsymbol{a}$ we get simplified formula for diffraction at a one-dimensional crystal of N scattering centers. The intensity is therefore the square of the absolute value

$$\left|S_{0,N}\right|^2 = \frac{\sin^2\left(N\, x/2\right)}{\sin^2\left(x/2\right)} \quad . \tag{2.56}$$

This distribution is also known as N-slit function. An example with $N = 6$ is shown in Fig. 2.11. Noteworthy are the (periodically ordered) main maxima and characteristic fringes between these maxima. Considering that these fringes occur due to diffraction at one-dimensional crystalline structures, it is not surprising that they are a common phenomenon in XRD.

2.3.6 Diffraction at an infinite crystal

For an infinite number of scattering centers (slits), the N-slit function becomes just a periodical ordering of δ-peaks. The resulting amplitude is

$$A\left(\boldsymbol{q}\right) = A_0\, C\, F\left(\boldsymbol{q}\right) \sum_h \sum_k \sum_l \delta\left(\boldsymbol{q}\cdot\boldsymbol{a} - 2\pi\, h\right) \delta\left(\boldsymbol{q}\cdot\boldsymbol{b} - 2\pi\, k\right) \delta\left(\boldsymbol{q}\cdot\boldsymbol{c} - 2\pi\, l\right) \;, \tag{2.57}$$

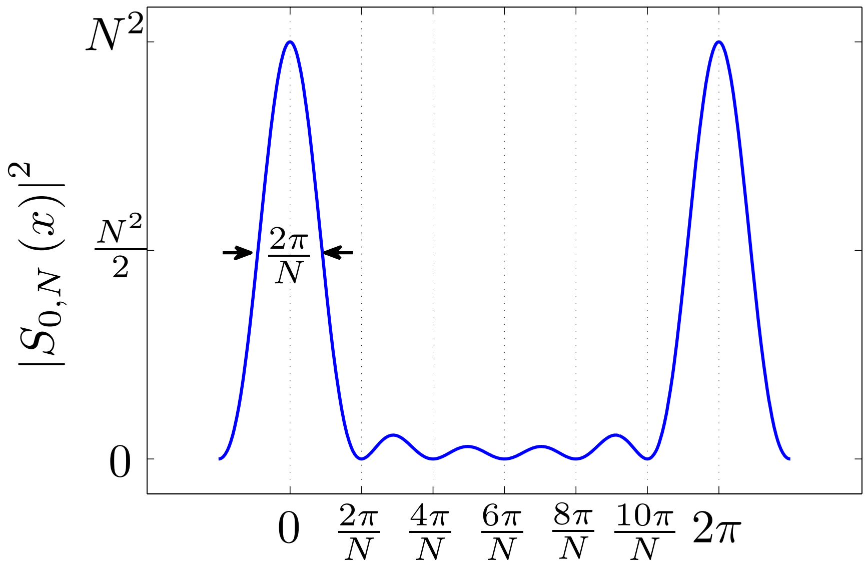

Figure 2.11: N-slit function for $N = 6$, image taken from [19]. $N - 2$ fringes occur between the main maxima at $x = 0$ and $x = 2\pi$. These are typical of diffraction patterns originating from one-dimensional periodically ordered scattering centers.

as shown in [20]. The well known Laue equations

$$\boldsymbol{q} \cdot \boldsymbol{a} = 2\pi\ h \tag{2.58}$$

$$\boldsymbol{q} \cdot \boldsymbol{a} = 2\pi\ k \tag{2.59}$$

$$\boldsymbol{q} \cdot \boldsymbol{a} = 2\pi\ l \tag{2.60}$$

follow obviously and describe the δ-peaks of the intensity distribution, which is equivalent to the amplitude distribution in this special case, of a wave diffracted at an infinite three-dimensional crystal.

Beside these maxima, the intensity is zero. The maxima of (theoretically) infinite intensity are called Bragg peaks, because the Bragg condition is fulfilled for the respective scattering vectors. In analogy to the crystal lattice, which describes the position of atoms in a crystal, a *reciprocal* lattice is introduced which describes the position of Bragg points in the *reciprocal* space. The primitive vectors of the latter *reciprocal* space can be formulated using the primitive vectors of the real space unit cell and the real space unit cell volume $V_E = \boldsymbol{a} \cdot (\boldsymbol{b} \times \boldsymbol{c})$. The resulting primitive reciprocal unit cell vectors

$$\boldsymbol{a}^* = \frac{2\pi}{V_E} (\boldsymbol{b} \times \boldsymbol{c}) \tag{2.61}$$

$$\boldsymbol{b}^* = \frac{2\pi}{V_E} (\boldsymbol{c} \times \boldsymbol{a}) \tag{2.62}$$

$$\boldsymbol{c}^* = \frac{2\pi}{V_E} (\boldsymbol{a} \times \boldsymbol{b}) \tag{2.63}$$

can be used to describe scattering vectors $\boldsymbol{q}$ as linear combination of these same reciprocal unit cell vectors

$$\boldsymbol{q} = H\,\boldsymbol{a}^* + K\,\boldsymbol{b}^* + L\,\boldsymbol{c}^* \ . \tag{2.64}$$

Understanding of the scattering vectors is simplified enormously by this view of the reciprocal space. The Bragg condition is usually fulfilled if H, K and L are integers. As a result, Bragg points and reciprocal unit cell vectors serve as orientation in the reciprocal space in the same way as atom positions and unit cell vectors do in real space.

2.3.7 Diffraction at a semi-infinite crystal

For practical purposes, infinite crystals are usually not suitable to model real crystal systems in XRD. This is not primarily because the crystal is too small to be considered of infinite size, but rather because the penetration depth of the X-rays is too small. Absorption leads to the fact that scattering at the atoms of layers farer away from the crystal surface is weaker compared to scattering at the topmost layers. This is why large crystalline parts of a sample, for example the substrate of a multi layer system, are viewed as *semi-infinite* perpendicular to the surface and *infinite* in the two dimensions parallel to the surface. In contrast to the model of an *infinite* crystal, this model of a *semi-infinite* crystal is suitable for crystals that are of large depth compared to the penetration depth of the X-ray beam.

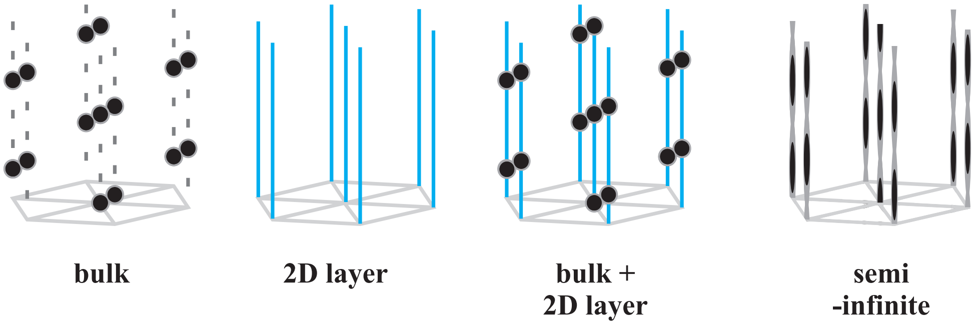

Figure 2.12: Diffraction at different crystal structures, image taken from [20] and revised. The intensity distribution of a wave diffracted at a *bulk* crystal gives high intensity only at the (zero-dimensional) Bragg spots. A two-dimensional surface (*2D layer*) gives an only two-dimensional Bragg condition, so that the diffracted intensity has a one-dimensional distribution. A two-dimensional surface on an infinite bulk crystal gives a combination of the two diffraction patterns. A semi-infinite crystal causes Bragg spots that are not perfectly sharp perpendicular to the surface. The resulting diffraction patterns are called *Crystal Truncation Rods* (CTRs).

Furthermore, surface roughness has to be taken into account. The amplitude for diffraction at a semi-infinite crystal with surface roughness is

$$A(\boldsymbol{q}) = A_0\, C\, \frac{1}{N_1 N_2} F(\boldsymbol{q}) \sum_{n_1=-\infty}^{\infty} e^{i\, n_1\, \boldsymbol{q}\cdot\boldsymbol{a}} \sum_{n_2=-\infty}^{\infty} e^{i\, n_2\, \boldsymbol{q}\cdot\boldsymbol{b}} \sum_{n_3=-\infty}^{N_3(n_1,n_2)} e^{i\, n_3\, \boldsymbol{q}\cdot\boldsymbol{c}}\, e^{i\, n_3 \epsilon} \tag{2.65}$$

$$= A_0\, C\, \frac{1}{N_1 N_2} F(\boldsymbol{q}) \sum_{n_1=-\infty}^{\infty} e^{i\, n_1\, \boldsymbol{q}\cdot\boldsymbol{a}} \sum_{n_2=-\infty}^{\infty} e^{i\, n_2\, \boldsymbol{q}\cdot\boldsymbol{b}} \sum_{n_3=-\infty}^{N_3(n_1,n_2)} e^{i\, n_3\, (\boldsymbol{q}\cdot\boldsymbol{c} + \epsilon)}\, . \tag{2.66}$$

The term $e^{i\, n_3 \epsilon}$ for the direction perpendicular to the surface contains the damping factor ϵ, which lessens the influence of layers further away from the crystal surface. This accommodates the absorption effect mentioned above. $N_3(n_1, n_2)$ gives the number of layers at a lateral position (n_1, n_2) and thereby describes the roughness of the surface (cf. Fig. 2.13).

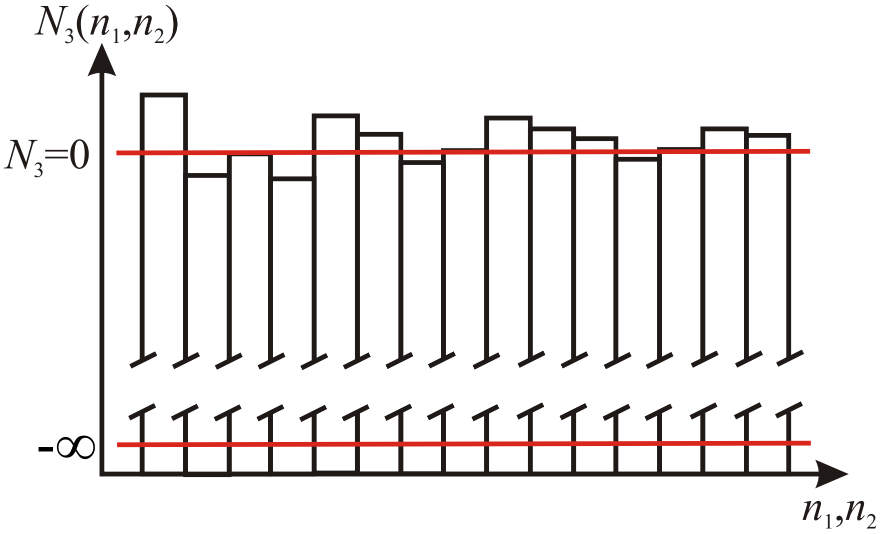

Figure 2.13: Surface roughness of a semi-infinite crystal, image taken from [19]. Different layer numbers N_3 at different lateral coordinates (n_1, n_2) describe the surface roughness.

In this work, we assume that the crystal is of infinite size parallel to the surface and thus that all reflected intensity is located at the Crystal Truncation Rods (CTRs). Furthermore, the calculations are done only for the CTRs and we assume pseudomorphic growth for the films on top of the substrate, so that the CTRs of the crystalline structures are exactly on top of each other. Factoring in the Laue equations 2.61 and 2.62, we can then describe the amplitude as

$$A\left(\boldsymbol{q}\right) = A_0\, C\, \frac{1}{N_1 N_2} F\left(\boldsymbol{q}\right) \sum_{n_1=-\infty}^{\infty} 1 \sum_{n_2=-\infty}^{\infty} 1 \sum_{n_3=-\infty}^{N_3(n_1,n_2)} e^{\,i\, n_3\, (\boldsymbol{q}\cdot\boldsymbol{c} + \epsilon)} \tag{2.67}$$

$$= A_0\, C\, \frac{1}{N_1 N_2} F\left(\boldsymbol{q}\right) \sum_{n_1=-\infty}^{\infty} \sum_{n_2=-\infty}^{\infty} \frac{e^{\,i\, N_3(n_1,n_2)\, (\boldsymbol{q}\cdot\boldsymbol{c} + \epsilon)}}{1 - e^{-(i\,\boldsymbol{q}\cdot\boldsymbol{c} + \epsilon)}} \tag{2.68}$$

$$= A_0\, C\, \frac{1}{N_1 N_2} F\left(\boldsymbol{q}\right) \frac{\left\langle e^{\,i\, N_3(n_1,n_2)\, (\boldsymbol{q}\cdot\boldsymbol{c} + \epsilon)} \right\rangle}{1 - e^{-(i\,\boldsymbol{q}\cdot\boldsymbol{c} + \epsilon)}}\ . \tag{2.69}$$

We now assume function $N_3(n_1, n_2)$ to be a Gaussian distribution and can calculate the averaging part of the above function as

$$\left\langle e^{\,i\, N_3(n_1,n_2)\, (\boldsymbol{q}\cdot\boldsymbol{c} + \epsilon)} \right\rangle \equiv \int_{-\infty}^{\infty} dn_3 \frac{1}{\sigma\sqrt{2\pi}}\, e^{-\frac{\left(n_3-\overline{N_3}\right)^2}{2\sigma^2}}\, e^{n_3\, (i\,\boldsymbol{q}\cdot\boldsymbol{c} + \epsilon)} \tag{2.70}$$

$$= e^{-\frac{\sigma^2 (\boldsymbol{q}\cdot\boldsymbol{c})^2}{2}}\, e^{\overline{N_3}\, (i\,\boldsymbol{q}\cdot\boldsymbol{c} + \epsilon)}\ . \tag{2.71}$$

The standard deviation σ describes the surface roughness. By setting the arbitrary average thickness $\overline{N_3}$ to zero, one can simplify the amplitude of a wave diffracted at a semi-infinite crystal to

$$A\left(\boldsymbol{q}\right) = A_0\, C\, F\left(\boldsymbol{q}\right) \frac{e^{-\sigma^2\, (1 - \cos\left(\boldsymbol{q}\cdot\boldsymbol{c}\right))}}{1 - e^{-\,(i\,\boldsymbol{q}\cdot\boldsymbol{c} + \epsilon)}}\ . \tag{2.72}$$

2.3.8 Diffraction at a thin film

Thin and ultrathin films of several unit cell layers require the assumption of roughnesses both at the top side and at the bottom side of the respective film. This is simply because, in contrast to a semi-infinite substrate crystal, the amplitude diffracted at the bottommost layers of the film and at layers even below those (e.g. at the substrate) is *not* infinitesimal due to damping effects. We also assume that the penetration depth of the X-ray beam is large compared to the film thickness, so that absorption is not significant and the damping factor ϵ can be set to zero. From eq. 2.52, we consequently get

$$A\left(\boldsymbol{q}\right) = A_0\, C\, \frac{1}{N_1 N_2} F\left(\boldsymbol{q}\right) \sum_{n_1=-\infty}^{\infty} 1 \sum_{n_2=-\infty}^{\infty} 1 \sum_{n_3=N_3^-(n_1,n_2)}^{N_3^+(n_1,n_2)} e^{\,i\, n_3 \boldsymbol{q}\cdot\boldsymbol{c}}\ . \tag{2.73}$$

The roughness is described by $N_3^+(n_1, n_2)$ and $N_3^-(n_1, n_2)$ as shown in Fig. 2.14. Analogous to the conversions in chapter 2.3.7, we assume standard deviation of the film expansion and

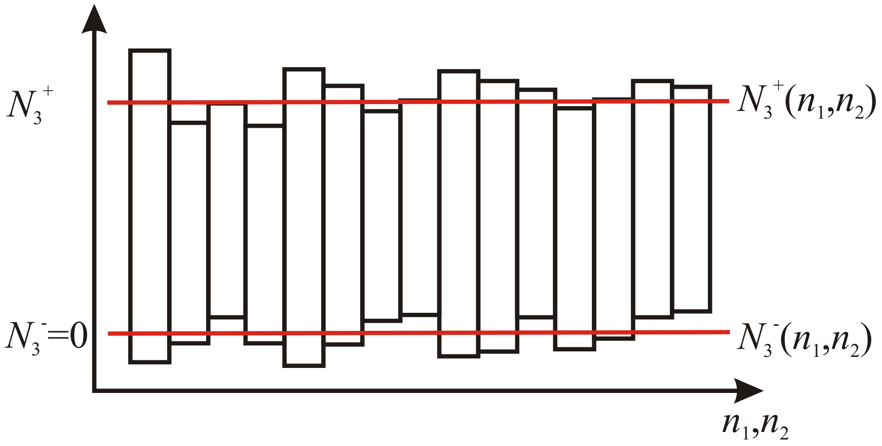

Figure 2.14: Roughness of a (ultra-)thin layer, image taken from [19]. The roughnesses at top and bottom is calculated assuming standard deviation of the film expansion in top direction $N_3^+(n_1, n_2)$ and bottom direction $N_3^-(n_1, n_2)$.

finally get an amplitude of the diffracted wave of

$$A\,(\boldsymbol{q}) = A_0\, C\, F\,(\boldsymbol{q})\, \frac{e^{-\sigma_-^2\,(1-\cos \boldsymbol{q}\cdot\boldsymbol{c})} - e^{i\,\overline{N_3}\,\boldsymbol{q}\cdot\boldsymbol{c}} \cdot e^{-\sigma_+^2\,(1-\cos \boldsymbol{q}\cdot\boldsymbol{c})}}{1-e^{i\,\boldsymbol{q}\cdot\boldsymbol{c}}}\,. \tag{2.74}$$

This is also shown in more detail in [20].

2.3.9 Diffraction at a crystalline system

As noted above, the substrates of the samples investigated in this work are assumed to be semi-infinite. In order to describe a crystalline system of one or more thin films plus a substrate, we can simply add up to diffracted amplitudes of the particular films and the substrate coherently, because we assume that no absorption takes place except in the substrate. Additionally, we introduce a fill factor θ_m, which accommodates empty space which can be created during the film deposition.[1]

---

[1] For practical purposes, it is also possible to correct inaccuracies of the declared model by choosing an appropriate fill factor θ_m. It is assumed that the films grow pseudomorphic, so that the CTRs in reciprocal space have identical lateral positions. This, however, is not always the case and it is not unusual to observe small deviations. The intensity measurements of the diffracted beam on a CTR normally follow the path of the CTR of the substrate because its intensity is usually stronger than the one of the films. Therefore, the measurement is slightly delocalized from the CTR of the films, which leads to smaller contribution of the film to the diffracted intensity than would be expected. This is an inaccuracy of the used model that can be compensated in simulations by adjusting the fill factor.

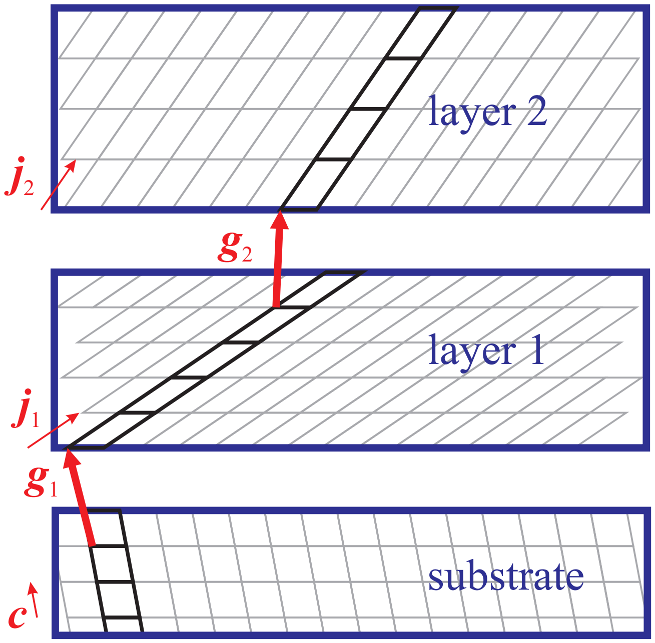

Figure 2.15: Schematic drawing of a crystalline system. Each layer m consists of a number of unit cells, which are shifted by $\boldsymbol{j_m}$, respectively. The bottom unit cell of a layer j is shifted from the topmost unit cell of the subjacent layer by $\boldsymbol{g_m}$.

The amplitude of a complex crystal system is

$$A(\boldsymbol{q}) = A_0\, C \Bigg(F_0(\boldsymbol{q}) \frac{e^{-\sigma^2 (1-\cos(\boldsymbol{q}\cdot\boldsymbol{c}))}}{1-e^{-(i\,\boldsymbol{q}\cdot\boldsymbol{c}+\epsilon)}} + \sum_{m=1}^{M} \theta_m\, e^{i\,\boldsymbol{q}\cdot\boldsymbol{p_m}}\, F_m(\boldsymbol{q}) \cdot \frac{e^{-\sigma^2_{-,m}(1-\cos\boldsymbol{q}\cdot\boldsymbol{j_m})} - e^{i\,\overline{N}_{3m}\,\boldsymbol{q}\cdot\boldsymbol{j_m}} \cdot e^{-\sigma^2_{+,m}(1-\cos\boldsymbol{q}\cdot\boldsymbol{j_m})}}{1-e^{i\,\boldsymbol{q}\cdot\boldsymbol{j_m}}} \Bigg), \tag{2.75}$$

with M different films m and the vertical unit cell vector $\boldsymbol{j}_m$, which stands for the distance between neighboring layers of a film. The phase vector

$$\boldsymbol{p_m} = \boldsymbol{g_m} + \sum_{m'=1}^{m-1} \boldsymbol{g_{m'}} + \overline{N}_{3m'} \cdot \boldsymbol{j_{m'}} \tag{2.76}$$

gives the phase of the film, which depends on the interface distance vector $\boldsymbol{g_m}$ and on phase shifts $\overline{N}_{3m'} \cdot \boldsymbol{j_{m'}}$ originating from the layers below the current one (cf. Fig 2.15).

2.3.10 Debye-Waller factor

For temperatures higher than 0 Kelvin, atoms in a solid vibrate about their (equilibrium) positions. This has an effect on the amplitude and thus intensity of a wave diffracted at such a structure. The effect is easily understandable by reconsidering Fig. 2.10, which shows the Bragg condition for XRD. If the Bragg condition is fulfilled, the amplitudes of the waves diffracted at the different layers interfere constructively. This condition is of course softened if single atoms of these layers are delocalized from their lattice positions. This is exactly what happens for temperatures higher than 0 Kelvin, although in this case the delocalization is not by a fixed margin but is rather a statistical process.

According to [21], this effect can be taken care of by introducing the so called Debye-Waller factor. With the delocalization of an atom from its equilibrium position $\boldsymbol{u}(t)$, the statistically modified structure factor is

$$\overline{F(\boldsymbol{q})} = \sum_{j=1}^{N} f_j(q)\, \overline{e^{i\,\boldsymbol{q}\cdot(\boldsymbol{r}_j+\boldsymbol{u})}} \tag{2.77}$$

$$= \overline{e^{i\,\boldsymbol{q}\cdot\boldsymbol{u}}} \sum_{j=1}^{N} f_j(q)\, e^{i\,\boldsymbol{q}\cdot\boldsymbol{r}_j} \tag{2.78}$$

and can be developed to

$$\overline{F(\boldsymbol{q})} = e^{-\frac{1}{6}\,|\boldsymbol{q}|^2\,\overline{|\boldsymbol{u}|^2}} \sum_{j=1}^{N} f_j(q)\, e^{i\,\boldsymbol{q}\cdot\boldsymbol{r}_j} \ . \tag{2.79}$$

After [17], we define the Debye-Waller factor as

$$D = \frac{1}{6}\overline{|\boldsymbol{u}|^2} \tag{2.80}$$

and end up with a modified structural form factor

$$\overline{F(\boldsymbol{q}, D)} = e^{-D\,|\boldsymbol{q}|^2} \sum_{j=1}^{N} f_j(q)\, e^{i\,\boldsymbol{q}\cdot\boldsymbol{r}_j} \ , \tag{2.81}$$

which depends noticeably on the Debye-Waller factor for high scattering vectors. As our measurements were carried out at room temperature, the expected influence of the Debye-Waller factor is limited. However, analogous to the fill factor θ_m introduced above, the Debye-Waller factor can also be used to simulate other effects, which are not included in our model. This is especially the case for the effect of point defects, because the intensity drop for higher scattering vectors is of the same dimension as the one of the Debye-Waller factor. This may lead to unrealistically high Debye-Waller factors and accordingly unrealistically high simulated temperatures in certain cases, up to temperatures where the sample would no longer be solid. If used properly, fitting the Debye-Waller factor can albeit provide interesting information about the investigated samples, e.g. hints to point defects, as mentioned above.

2.4 X-ray photoelectron spectroscopy

X-ray photoelectron spectroscopy (XPS) is a well established quantitative technique in surface science. It is based on the photoelectric effect and can be used to determine the empirical formula as well as the chemical and electronic state at the surface of a material. XPS plays a minor role in the results presented in this work. Therefore, it will not be discussed as intensively as XRR and XRD in this theoretical part. However, a brief introduction will be given, that is sufficient to understand the results obtained and discussed in this work.

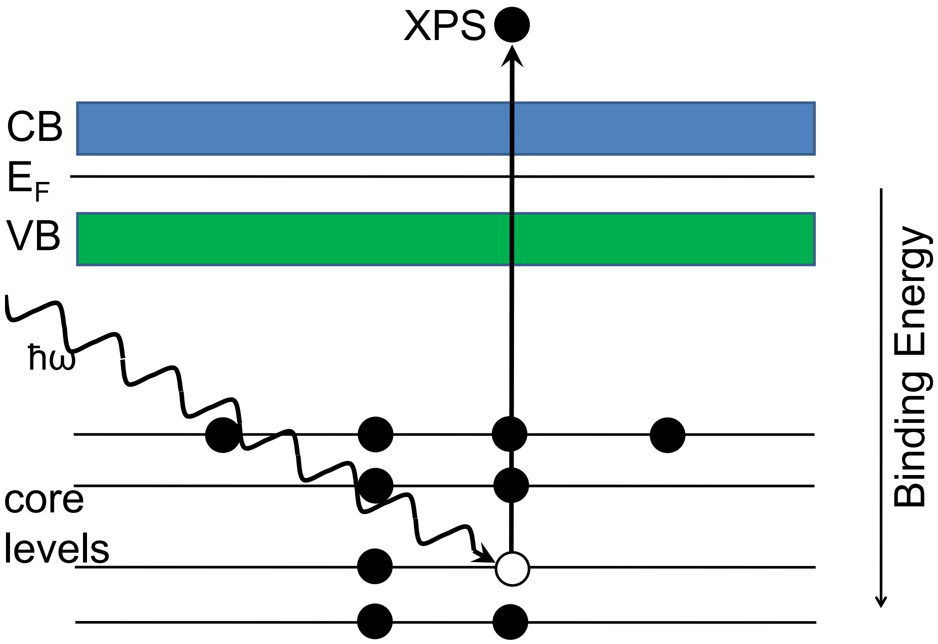

Figure 2.16: Scheme of X-ray photoelectron spectroscopy, image taken from [22]. A photon hits a core electron and transfers its energy to this electron. Part of the former photon energy is used to overcome the binding energy, the rest of the energy becomes the kinetic energy of the now free electron.

In XPS, a sample is exposed to X-rays. If a photon is absorbed by an electron of an atom, the photon energy E_{photon} may be more than needed by the electron to overcome the effective binding energy $E_{B,eff}$ of the atom for this particular electron plus the work function ϕ of the *spectrometer*. By measuring the resulting kinetic energy of the photon $E_{kinetic}$, the former binding energy can thus be calculated by

$$E_{B,eff} = E_{photon} - \phi - E_{kinetic} \ . \tag{2.82}$$

It is important to note that this formula is only correct if the sample is conductive and grounded to the same potential as the spectrometer, so that the Fermi level of sample and spectrometer valance band are the same. This is explained in more detail in [23]. If the sample is not grounded properly, e.g. because it is an insulator, this additional work function must also be taken into account. This is especially true for samples of Si with an insulator on top, like the samples investigated in this thesis.

As shown above, the former binding energies of emitted electrons can be determined via XPS. As these energies are characteristic of specific elements, an elemental analysis is possible. Because the effective binding energy is slightly modified by the chemical binding of the atom with neighboring atoms and also of the remaining atoms of the sample, these binding energies are shifted slightly from the theoretical values of a single atom. Therefore, XPS also gives information about the chemical state of the detected atoms.

In addition to the binding energies discussed above, additional satellite peaks are detected in XPS. The kinetic energy of the photoelectron can also be used to transfer another electron to an orbital of higher energy in a *shake up* process or to even remove in completely it a *shake off* process. The missing kinetic energy of the emitted photoelectron therefore causes an additional intensity *satellite* peak with a higher binding energy in the calculated binding energy spectrum.

Furthermore, Auger lines are visible in the XPS spectrum. If an electron is emitted from an atom in XPS, the electron is replaced by another electron. The free energy originating from this process is transferred to another electron. If the energy is higher than the binding energy of this atom, another free electron is released, with a kinetic energy that is also characteristic for the binding energies of the involved electrons.

2.5 Investigated materials

This work is about X-ray structure analysis of thin praseodymium oxide films on Si(111). Obviously, it makes sense to present the known facts about the involved materials prior to this work. Both praseodymium oxide and Si have been investigated extensively. The results for Si were of high definiteness and it is non-exaggerated to state that Si is in principle well understood. The same is unfortunately not true for praseodymium oxide, as can be seen from the strong differences of density and unit cell size determined by different authors for alleged identical crystalline structures.

2.5.1 Silicon(111)

Si is the second most abundant element in the crust of earth. This is mostly in the form of SiO_2, but Si is also present in various other compounds. Ultra-pure Si is used to produce Si wafers for electronic applications. These ultra-pure Si semiconductors can be doped with other elements to tune their electrical properties in a wide range. Because Si keeps its semiconducting properties even at high temperatures and since its native oxide forms an extremely sharp semiconductor/dielectric interface, Si has become a de facto standard for the semiconductor industry.

Si is a semi-metal which has the atomic number 14 and a melting point of 1414°C. It crystallizes in diamond cubic structure, that means two face-centered cubic lattices, which are separated by 1/4 of the unit cell width in each dimension. The unit cell therefore consists

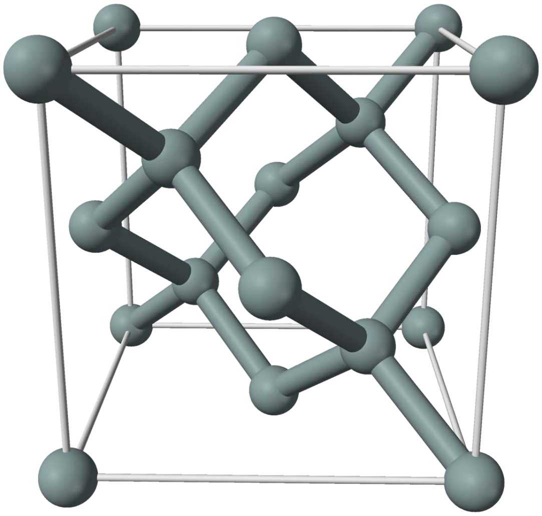

Figure 2.17: Si unit cell, image taken from [24]. Two face-centered unit cells, separated by 1/4 of the unit cell width in each dimension, form the diamond structure.

of $2 \cdot 4 = 8$ atoms with a lattice constant of 5.4307 Å. A schematic drawing of the unit cell is shown in Fig 2.17.

In this work, boron-doped silicon wafers with (111) surface and a thickness of $(525 \pm 15)\mu m$ are used as substrate for praseodymium oxide films. The miscut of the surface is $(0.35 \pm 0.15)^\circ$ and the dopant concentration dependent resistivity is between 5 Ωcm and 15 Ωcm.

The surface unit cell of Si(111) is of special importance for this work because the epitaxial relationship between Si and praseodymium oxide depends on the surface unit cells and not directly on the bulk unit cells. This surface unit cell has a six-fold rotational symmetry with the rotation axis perpendicular to the surface. The lateral lattice constant is 3.8401 Å, while the vertical lattice constant is 3.1354 Å. The symmetry reduces to three-fold if one takes into account the different vertical position of the surface atoms. This is the reason why in XRD measurements, the symmetry is only three-fold in contrast to, for example, low energy electron diffraction (LEED), where only two-dimensional diffraction takes place.

Surface reconstruction takes place at clean Si surfaces in Ultra High Vacuum (UHV) and superstructures are formed. These reconstructions will not be explained here, as they disappear when the praseodymium oxide film is adsorbed.

2.5.2 Praseodymium oxide

Praseodymium is a rare earth element with the atomic number 59 and a melting point of 935°C. It is a strong oxidant and occurs in oxidation stages +3 and +4. The resulting oxides range from $Pr_2O_3 = PrO_{1.5}$ to PrO_2 and have been investigated as bulk crystals for decades.

Ever since then, distinguishing between the different oxidation stages and phases has appeared to be problematic. The more investigations were made, the more intermediate phases were found, which were similar but not identical in structure and size. The small differences in unit cells ended in larger and more complicated unit cells, and the progress peaked preliminary in stoichiometries like $Pr_{88}O_{160}$ [25]. In addition, stoichiometries that were thought to be understood appeared to be more complex than originally thought, and reports about Pr_6O_{11} [26] were followed by larger structures of identical composition stoichiometry like $Pr_{12}O_{22}$ and $Pr_{24}O_{44}$ [27].

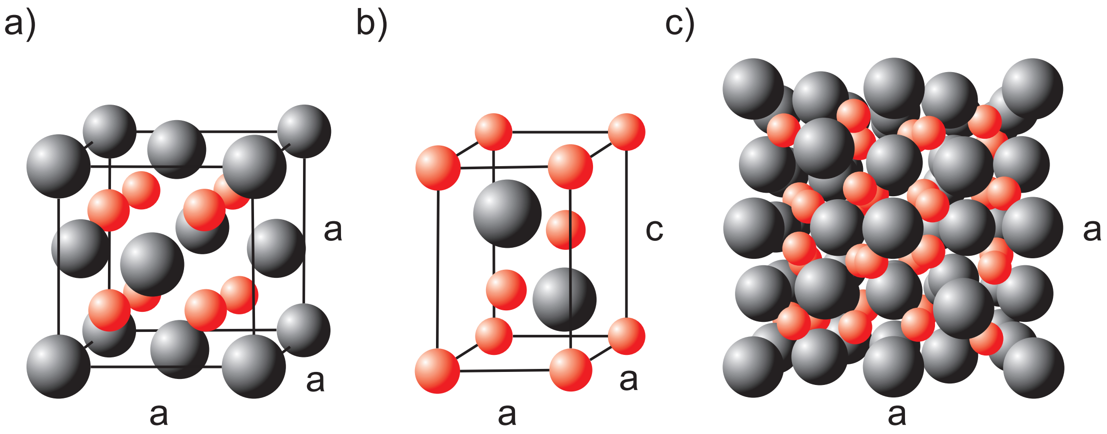

Figure 2.18: Unit cells of (from left to right) c-PrO_2, h-Pr_2O_3 and c-Pr_2O_3, image taken from [28]. The latter is basically identical to c-PrO_2, but has periodically ordered oxygen vacancies. Praseodymium atoms are shown in black color, oxygen atoms in red color.

These results are not meant to be played down here. But the problem with these kind of results is that they are probably not completely transferable to thin film structures, which are the topic of this work. The point is that surface effects, e.g. strain, must be taken into account for practical purposes. An oxide that is as sensitive to changes of ambient oxygen pressure and temperature cannot be expected to behave identically as bulk crystal and as thin (strained) film with possible impurities.

Regardless of the many different phases, only three phases are commonly mentioned. These are hexagonal h-Pr_2O_3, cubic c-Pr_2O_3 and cubic c-PrO_2 (cf. Fig. 2.18). Rudenko *et al.* [29] also state that praseodymium oxide tends to coexist in different oxidation stages and that the stoichiometries from $PrO_{1.5}$ to $PrO_{2.0}$ are essentially fluorite c-PrO_2 structures with oxygen vacancies. Due to the periodic arrangement of these vacancies, superstructures are formed. Rudenko *et al.* furthermore show that c-Pr_2O_3 is only energetically favorable compared to h-Pr_2O_3 if excess oxygen is present, and should therefore strictly speaking be called c-$Pr_2O_{3+\delta}$.

A detailed overview of the oxidation process concerning equilibrium stoichiometries and (de-)oxidation kinetics is given in [30]. The process depends on partial oxygen pressure, temperature and, of course, time.

2.5.3 Praseodymium oxide on silicon(111)

Previous studies show that under ultra high vacuum (UHV) conditions, praseodymium oxide grows in the hexagonal phase and (0001) orientation on Si(111) substrate with a substrate temperature of 625°C [31, 32]. For the experiments shown and discussed in this work, the evaporation is done via molecular beam epitaxy (MBE) and the growth rate is about 0.1 nm/s, unless otherwise stated.

It was shown that such h-Pr_2O_3 films of 5 nm thickness are converted to twin-free c-Pr_2O_3 when annealed in 10^{-5} mbar oxygen [33] or 1 atm nitrogen with oxygen partial pressure of 10^{-5} mbar [34] for 30 minutes. The temperatures during the post deposition annealing (PDA) process were 600°C and 700°C, respectively. These results are also summarized in [4]. From bulk experiments, however, it is probable that the phase transition takes place at lower temperatures as well. The exact temperature that is needed is hard to quantify from the given results, but it can be expected that it also depends on time and oxygen pressure.

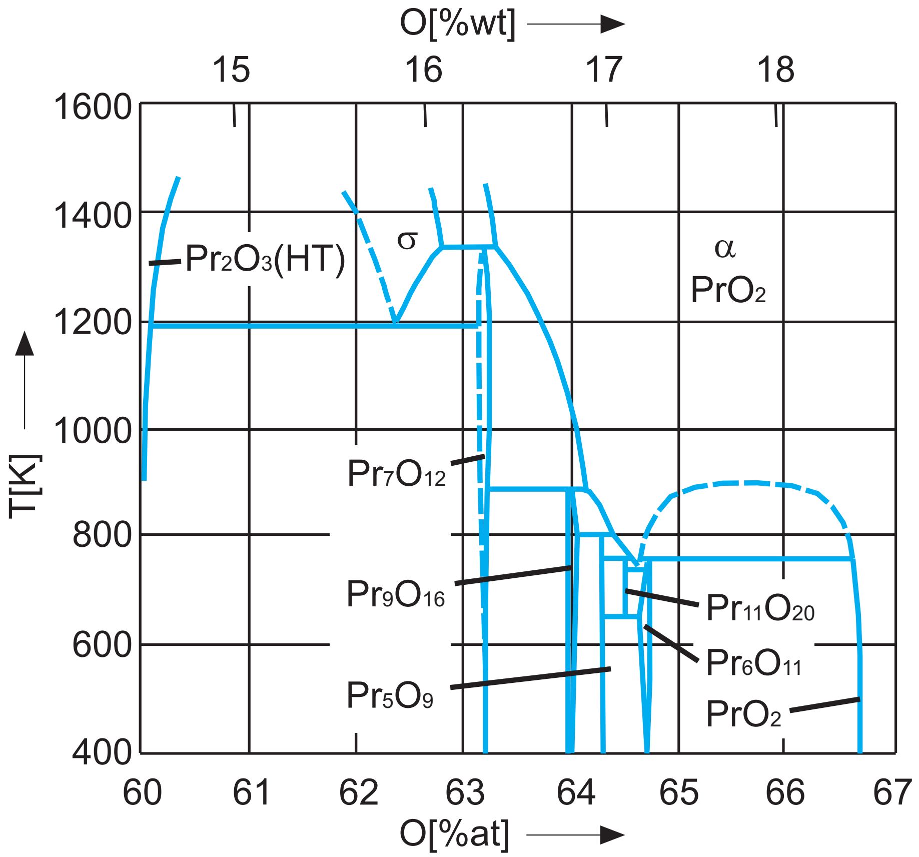

Figure 2.19: Partial phase diagram of *bulk* praseodymium oxide, image taken from [28]. Illustrated are the equilibrium stoichiometries, which depend on temperature and oxygen ambient pressure.

The most prominent praseodymium oxide surface unit cells fit the Si surface unit cell very well in terms of the lateral lattice constants.

- (111) oriented c-Pr_2O_3 has a lateral surface unit cell size of 15.772 Å (410.6% of Si(111)).

- (0001) oriented h-Pr_2O_3 has a lateral lattice constant of 3.859 Å (100.5% of Si(111)).
- (111) oriented c-PrO_2 has a lateral lattice constant of 3.813 Å (99.3% of Si(111)).

In the case of (111) oriented c-Pr_2O_3, the lateral unit cells of praseodymium oxide and Si do no fit directly, but c-Pr_2O_3 fits an arrangement of two Si unit cells. Because of that, c-Pr_2O_3 tends to form antiphase domains on Si(111). Since antiphase domain boundaries are disadvantageous for heteroepitaxial films, h-Pr_2O_3 and c-PrO_2 might seem to be more desirable. However, as h-Pr_2O_3 tends to form hydroxides, c-PrO_2 remains as the praseodymium oxide of choice on Si(111).

For XRR analysis, the respective δ and β values of the investigated materials, which describe the index of refraction, are of importance. Exact values for praseodymia are usually not given in literature, the densities in the following tables are therefore calculated from the unit cell sizes of the different species, except for cubic PrO_2, which is from [35]. Using theses values for densities, δ and β are calculated via an online calculator [36].The calculations assume a lattice constant of 5.394 Å for four PrO_2 molecules and hence a volume of V = 156.9 Å^3 and hexagonal lattice constants of $a = 3.975$ Å and $c = 6.31$ Å for a h-Pr_2O_3 cell, resulting in a volume of V = 86.3 Å^3. 16 c-Pr_2O_3 molecules have a lattice constant of $a = 11.152$ Å and thus a volume of V = 1387 Å^3[35]. The calculations of δ and β were done for photon energies of 10 keV.

substance	density$[\frac{g}{cm^3}]$	δ	β
c-PrO_2	7.30	1.307E-05	1.325E-06
c-Pr_2O_3	6.30	1.119E-05	1.197E-06
h-Pr_2O_3	6.33	1.124E-05	1.203E-06
Si	2.329	4.887E-06	7.376E-08
SiO_2(amorphous)	2.2	4.6E-06	3.9E-08
SiO_2(crystalline)	2.6	5.4E-06	4.6E-08

The cubic or pseudocubic species between c-PrO_2 and c-Pr_2O_3 can be expected to have monotonously decreasing densities because the distance between the praseodymium atoms also decreases, while the number of oxygen vacancies increases. In XRR analysis, however, even PrO_2 and c-Pr_2O_3 are hardly distinguishable, as shown in Fig. 2.20. The same is true for Si and SiO_2. Density and hence index of refraction are also different for amorphous and crystalline SiO_2.

Because a differentiation between the different praseodymia species based on XRR therefore seems to be unrealistical, two column models for laterally coexisting praseodymia species are not part of the simulations in the following chapters. This is of course only true for XRR. In XRD data, the different columns are in principle distinguishable, although an exact assignment to a concrete stoichiometry is not always possible. This is especially true for thin films, as the strain effects that occur here are not completely understood.

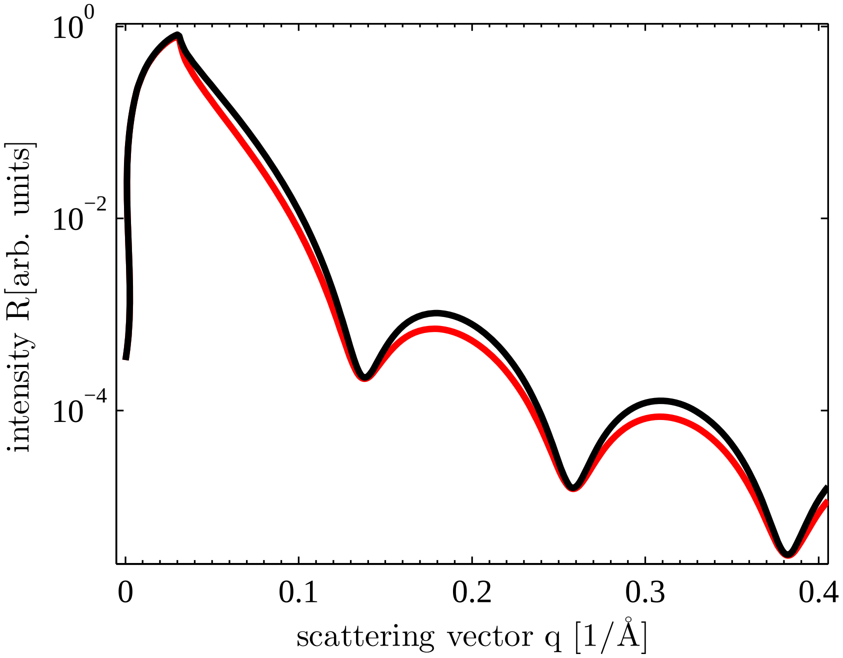

Figure 2.20: Simulated XRR data for PrO_2 (black line) and c-Pr_2O_3 (red line), assuming photon energies of 10 keV. The differences due to the different indices of refraction are very small.

Prior to this work, c-PrO_2 has never been prepared on Si(111). In the following chapters, the achievements of our workgroup in this context will be presented. Also, principle problems that occur during the deposition and oxidation as well as possible solutions will be discussed. In addition to this, a new analysis method for X-ray diffraction is presented, which was developed in the context of our praseodymium oxide on Si experiments, but is transferable to many other material systems that are investigated via X-ray diffraction.

3 Experimental setup

3.1 Sample preparation of praseodymium oxide on Si(111)

The praseodymium oxide on 4" Si(111) wafers investigated in this work were prepared by the IHP GmbH[2]. The substrates are single crystalline Si wafers, provided by the Siltronic AG[3]. The surface orientation is [111] with a miscut of $(0.35 \pm 0.15)^\circ$, mainly in $[1\bar{1}0]$ direction. It is noteworthy that this means that the miscut is never smaller than 0.20°, so that the mean terrace width is never extremely large. The wafers are doped with boron, resulting in a specific resistance of (5 - 15) Ωcm.

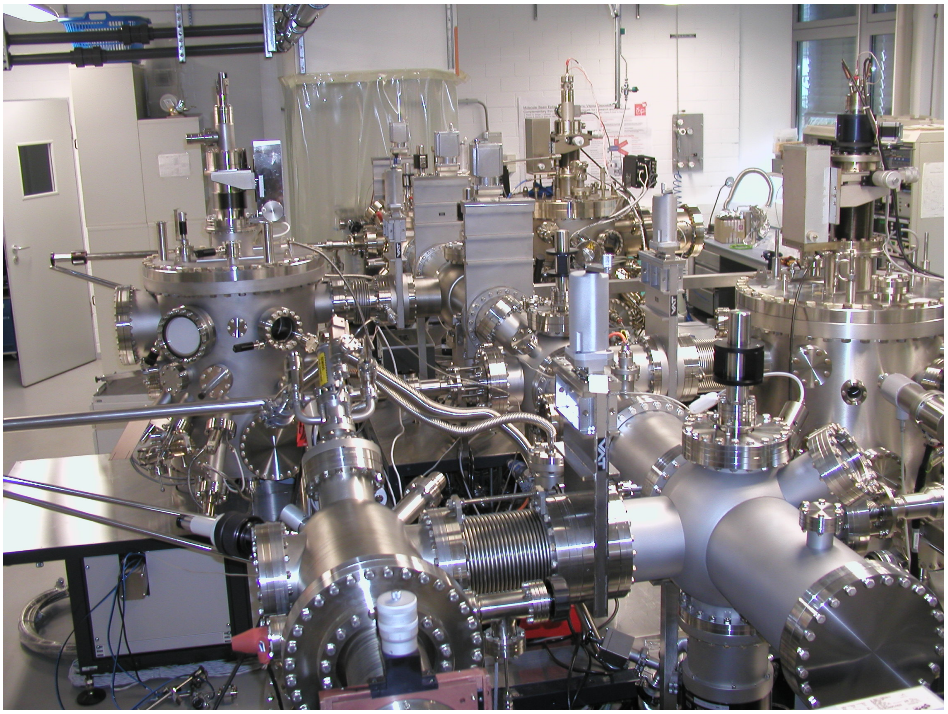

Figure 3.1: UHV chamber at the IHP in Frankfurt (Oder). The actual evaporation of praseodymium oxide takes place in the chamber at the lower right.

The substrates were cleaned by a combination of several techniques:

- Rinsing in DI water[4] for 10 minutes.

---

[2] IHP GmbH, Im Technologiepark 25, 15236 Frankfurt (Oder), Germany, `http://www.ihp-microelectronics.com/`

[3] Siltronic AG, Hanns-Seidel-Platz 4, 81737 Munich, Germany, `http://www.siltronic.com/`

[4] Deionized water. Water, which has had its minerals removed by specially-manufactured ion exchange resins which bind to and filter out the mineral salts from water.

- 10 minutes etching in piranha solution, in this case a mixture of 4:1 of sulfuric acid (H_2SO_4) and hydrogen peroxide (H_2O_2). Due to the exothermic mixing process, the temperature of the solution is about 80°C. Piranha cleaning is applied to decontaminate the wafers, especially from elemental carbon contaminations. The cleaning process is achieved by a fast dehydration and a slower oxidation process.

- Rinsing in DI water for 1 minute.

- Oxide removal in hydrogen fluorite solution, in this case in a mixture of HF:DI of 1:20 for 1 minute, leaving the surface Si atoms covalently bonded to hydrogen.

- Rinsing in DI water for 5 minutes.

- Washing in 40% ammonium fluoride ($[NH_4]F$) for 30 minutes in order to further reduce roughness. The result is an atomically sharp H-terminated surface of Si(111).

The technique of choice to study fundamental behavior and practicability of material systems is molecular beam epitaxy (MBE), although mass production is typically done via chemical vapor deposition (CVD). MBE was therefore used to prepare the samples investigated in this work.

Before the actual evaporation step, the sample and its holder were degassed in a high vacuum chamber at 200°C for 30 minutes. Afterwards, it was transferred to an ultra high vacuum deposition chamber, where it was heated up to 700°C to prepare a high quality (7×7) Si(111) surface.

The MBE system used was of type DCA 600. An electron beam was focused directly on the praseodymium oxide powder. This is clearly preferable compared to a heating of the crucible because praseodymium oxide powder is a very bad thermal conductor. Heating of the crucible, as it is done in [37, 38, 28], for example, therefore implicates very high crucible temperatures. This is especially problematic because crucibles made of tungsten[37] or molybdenum[38] tend to oxidize due to the oxygen provided by the praseodymium oxide, and these oxides evaporate at relatively low temperatures. A vapor pressure of 10^{-4} Torr is reached at 900°C for MoO_3 and at 980°C for WO_3, but only at 1400°C for Pr_2O_3 [39].

These problems do not occur if the oxide is heated directly. In the case of the samples investigated in this work, Pr_6O_{11} powder was reduced to Pr_2O_3 and then heated further to evaporate so that the growth rate on the sample is about 0.1 nm/s. The substrate was heated to 625°C and the pressure during evaporation was in the 10^{-8} mbar range. The crucible is made of pyrolytic graphite and the Si wafer was rotated during evaporation to cover for minor inhomogeneities of the particle beam.

The praseodymium oxide films prepared this way are twin-free and hexagonal, as shown in [32]. The film thickness is about 5 nm, and the samples were transferred to an oven with constant oxygen flow and oxygen pressure of 1 atm. Here, they were heated at different temperatures for 30 minutes. The resulting samples are investigated in this work.

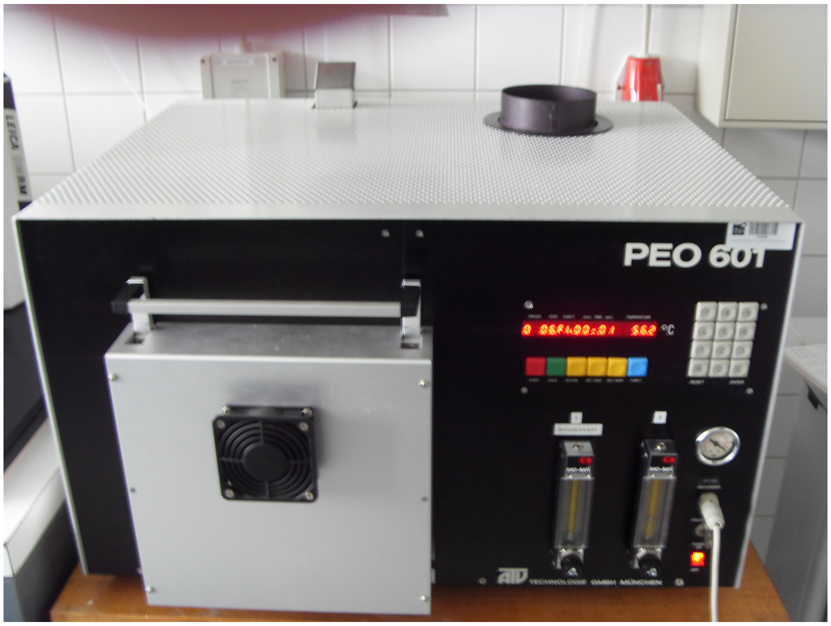

Figure 3.2: Furnace for post deposition annealing of the samples in oxygen. Temperatures were varied from sample to sample and the annealing time was 30 minutes.

3.2 Setup at HASYLAB

XRR, XRD and GIXRD (Grazing incidence X-ray diffraction) experiments presented in this work were performed at HASYLAB. The upgraded second generation synchrotron DORIS III acted as radiation source. DORIS III is exclusively used for the creation of synchrotron radiation since 1993. Positrons are accelerated to an energy of 4.45 GeV and brought onto a slalom course by wigglers, undulators and dipole magnets. The resulting synchrotron radiation is used to operate more than 30 beamline stations. Our experiments were performed at beamlines W1 and BW2, which are described in the following. Photon energies were 10.0 keV and 10.5 keV, corresponding to X-ray wavelengths of 1.24 Å and 1.18 Å.

3.2.1 Setup at beamline W1

Synchrotron radiation at beamline W1 is generated by a 32 pole wiggler (16 periods). At W1, the photon energy is adjusted using a Si double crystal monochromator and the beam size can be set by a system of motor controlled slits. The intensity can be damped via motor controlled absorber plates of different thicknesses that are moved into the beam according to requirements. This ensures that the diffracted intensity is always within detector limits.

Sample and detector are moved using a computer-controlled six circle diffractometer. The sample is aligned by detecting the related motor positions of linearly independent substrate Bragg peaks. At beamline W1, the motor movement during the measurements was limited, so that only the incidence angle and the reflected/refracted angle[5] were varied. Without tilting and rotating the sample, GIXRD measurements are impossible. Because of that, only

---

[5] Strictly speaking, the *detector* is moved, so that intensity reflected/refracted under certain angles is detected.

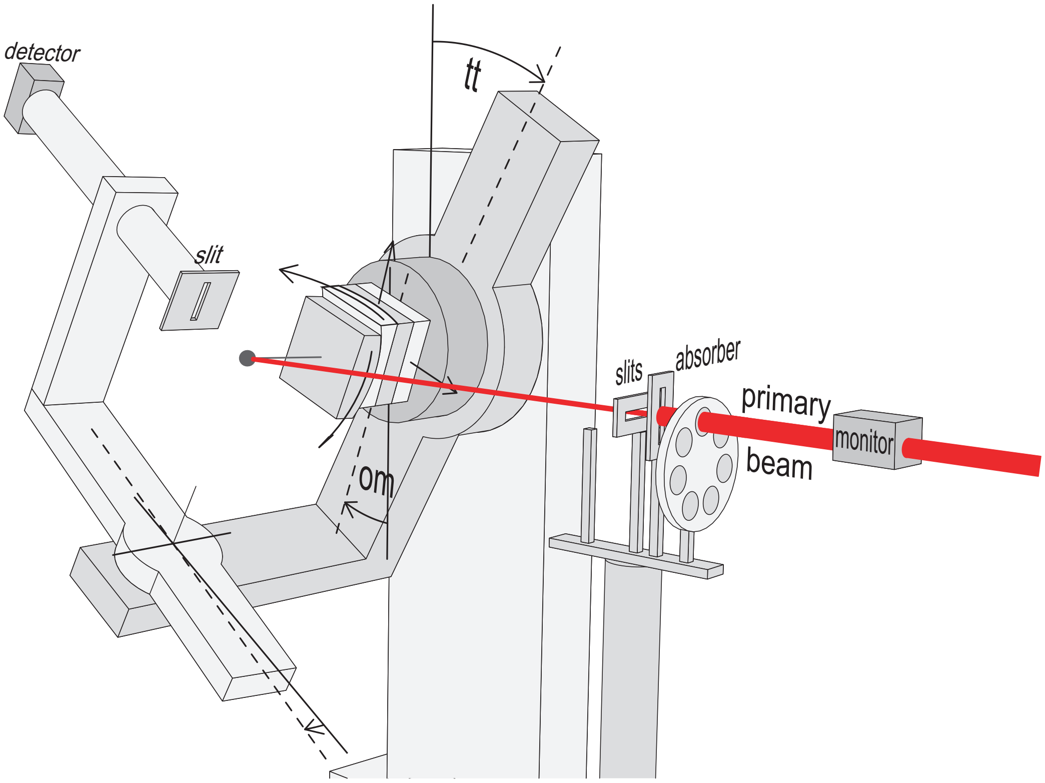

Figure 3.3: Six circle diffractometer, image taken from [40] and edited. The primary beam is damped by the absorber and reduced in size by slits, its intensity is controlled by the monitor. The beam is reflected/diffracted by the sample and the detector measures the intensity at a given position. During the XRR and XRD measurements, only incidence angle *om* and detector angle *tt* are moved. The remaining motors, indicated by the bent arrows, are only moved slightly and only during the alignment of the sample.

XRR and XRD measurements were performed at this beamline. The motor movements and calculations of reciprocal coordinates are done by a programm named *online*.

The alignment for XRR and XRD measurements differs slightly with respect to the surface of the sample. In the case of XRR, reflectivity at the different interfaces is measured. Therefore, the surface is along the top atoms of the sample, as one would expect from the term *surface*, so that the topmost interface between air and medium is defined as surface.

In XRD, this is not the case. The surface is defined by the crystal planes, which may differ slightly from the arrangement of the topmost atom layers, as shown in Fig. 3.4. This is because the actual surface defined by the topmost atoms does *not* play a role here. The Bragg Peaks are located perpendicular to the crystal planes. Therefore, the reciprocal space is also oriented at the crystal planes and hence at the unit cell vectors.

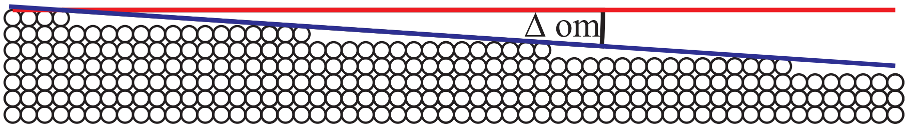

Figure 3.4: Miscut of a crystalline sample. The surface for XRR along the topmost atoms of the sample (blue line) differs slightly from the surface for XRD along the crystal planes (red line). The difference between these two directions Δ *om* is also called the *miscut* and is $(0.35 \pm 0.15)^\circ$ for the substrates used in this work.

3.2.2 Setup at beamline BW2

The radiation at beamline BW2 is generated by 56 pole wiggler (28 periods). Similar to the setup at W1, the setup at BW2 incorporates a Si double crystal monochromator, slits, a monitor and an adjustable absorber. Sample and and detector are also moved by a computer-controlled six circle diffractometer, but more degrees of freedom are used during the measurements. The sample is hit under a small fixed angle and measurements are performed for different scattering vectors. This implicates that the specular rod, with a scattering vector without lateral component, is not accessible in this setup, except for a single point where the diffracted angle equals the fixed incidence angle. The advantage of this grazing incidence X-ray diffraction (GIXRD) setup is that the *non* specular CTRs are widely accessible by rotation of the sample and the detector. The incidence angle is hence chosen with respect to the surface defined by the topmost atoms of the sample (XRR mode), and not by the crystal planes (XRD mode).

Motor movements and calculations of the reciprocal space are done by the program *tascom*.

3.3 RodsNPlots - an X-ray diffraction analysis tool

RodsNPlots is a graphical user interface (GUI) based simulation tool for X-ray diffraction (XRD) and Grazing incidence X-ray diffraction (GIXRD), which has been developed and improved in our workgroup in the context of this thesis. Diffraction at thin films with an underlying substrate can be simulated according to chapter 2.3. The program was used for the analysis of XRD and GIXRD data in [41, 42, 43, 17, 44, 19].

RodsNPlots was developed in [17] and is based on a programm developed in [20]. In *RodsNPlots*, the user creates a model of the simulated sample. A freely chosen number of crystalline films on a crystalline substrate is the basis of a model (cf. Fig 2.15). Each of these crystalline structures has a user-defined thickness, unit cell stretch factor, fill factor, layer distance, adsorption place, top and bottom roughness, and Debye-Waller factor (cf. [17] and chapter 2.3). These parameters are varied by different algorithms in limits specified by the user in order to achieve a best possible fit to the measured data. For practical purposes, the value for the layer thickness usually has to be set manually because the algorithms runs into local minima for a chosen layer thickness. However, setting this value manually was usually no problem for the samples investigated in this work as the value is normally obvious

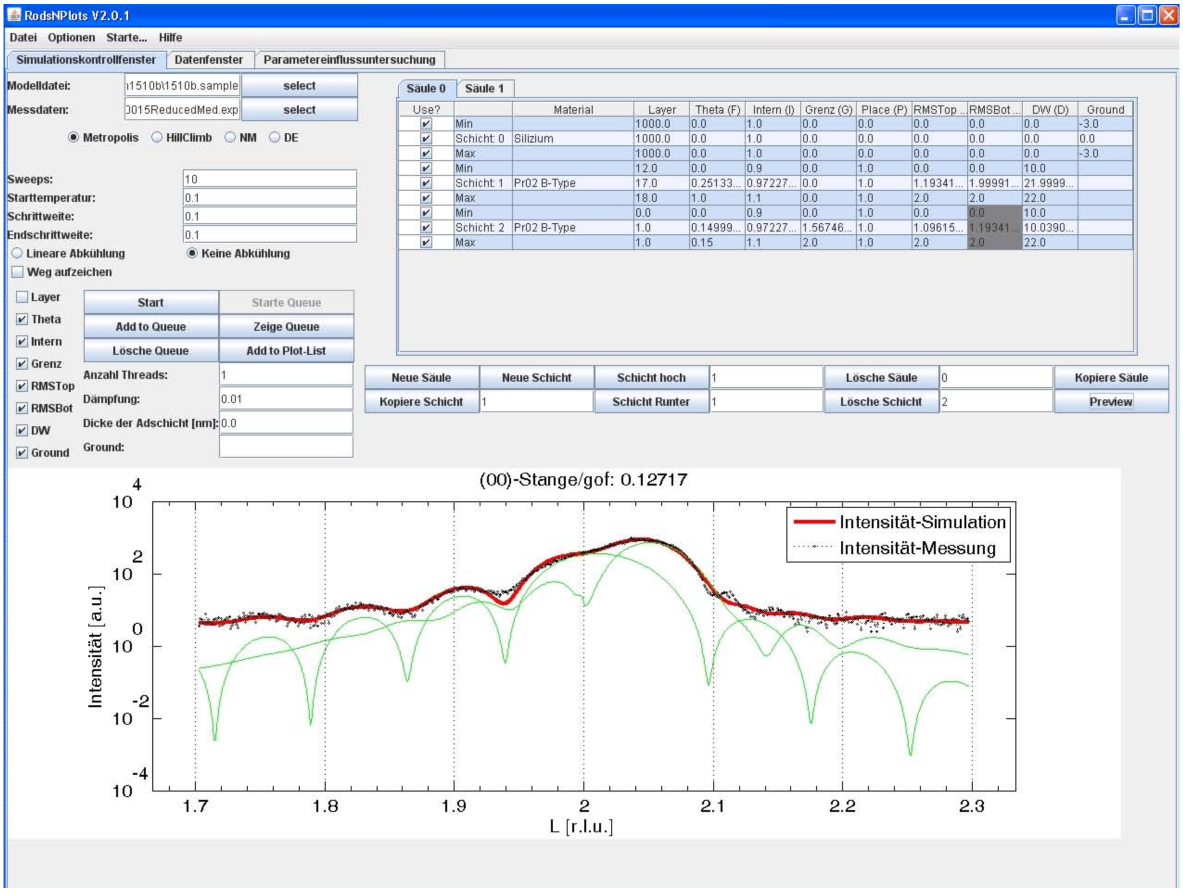
RodsNPlots V2.0.1
Datei
Optionen
Starte...
Hilfe
Simulationskontrollfenster
Datenfenster
Parametereinflussuntersuchung
select
select
Start
Starte Queue
Add to Queue
Zeige Queue
Lösche Queue
Add to Plot-List
Säule 0
Säule 1
Neue Säule
Neue Schicht
Schicht hoch
Lösche Säule
Kopiere Säule
Kopiere Schicht
Schicht Runter
Lösche Schicht
Preview
(00)-Stange/gof: 0.12717
Intensität-Simulation
Intensität-Messung
Intensität [a.u.]
L [r.l.u.]
10^4
10^2
10^0
10^{-2}
10^{-4}
1.7
1.8
1.9
2
2.1
2.2
2.3

Modelldatei: \1510b\1510b.sample
Messdaten:)015ReducedMed.exp
● Metropolis ○ HillClimb ○ NM ○ DE
Sweeps: 10
Starttemperatur: 0.1
Schrittweite: 0.1
Endschrittweite: 0.1
○ Lineare Abkühlung ● Keine Abkühlung
☐ Weg aufzeichen
☐ Layer
☑ Theta
☑ Intern
☑ Grenz
☑ RMSTop
☑ RMSBot
☑ DW
☑ Ground
Anzahl Threads: 1
Dämpfung: 0.01
Dicke der Adschicht [nm]: 0.0
Ground:

Use?		Material	Layer	Theta (F)	Intern (I)	Grenz (G)	Place (P)	RMSTop ...	RMSBot ...	DW (D)	Ground
☑	Min		1000.0	0.0	1.0	0.0	0.0	0.0	0.0	0.0	-3.0
☑	Schicht: 0	Silizium	1000.0	0.0	1.0	0.0	0.0	0.0	0.0	0.0	0.0
☑	Max		1000.0	0.0	1.0	0.0	0.0	0.0	0.0	0.0	-3.0
☑	Min		12.0	0.0	0.9	0.0	1.0	0.0	0.0	10.0	
☑	Schicht: 1	Pr02 B-Type	17.0	0.25133...	0.97227...	0.0	1.0	1.19341...	1.99991...	21.9999...	
☑	Max		18.0	1.0	1.1	0.0	1.0	2.0	2.0	22.0	
☑	Min		0.0	0.0	0.9	0.0	1.0	0.0	0.0	10.0	
☑	Schicht: 2	Pr02 B-Type	1.0	0.14999...	0.97227...	1.56746...	1.0	1.09615...	1.19341...	10.0390...	
☑	Max		1.0	0.15	1.1	2.0	1.0	2.0	2.0	22.0	

Schicht hoch: 1
Lösche Säule: 0
Kopiere Schicht: 1
Schicht Runter: 1
Lösche Schicht: 2

Figure 3.5: *RodsNPlots* screenshot. The top right area defines the model, the top left area sets the fitting algorithm. At the bottom, measured data (black dots) is compared to the calculated intensity distribution (red line) according to the model above. The individual intensity contributions of the two columns is shown by the green lines, respectively.

from the number of fringes (cf. Fig. 2.11).

During this work, it turned out that the investigated praseodymium oxide on Si samples could not be described sufficiently by these kinds of models. To simulate laterally coexisting species of praseodymium oxide, *RodsNPlots* was extended, so that suchlike structures can now be simulated by *multi column models* [41, 17]. The respective contribution of these columns is shown in the user GUI, as implemented in [44].

Hahne also implemented parameter coupling in *RodsNPlots* [44], so that certain parameters or their limits can be coupled to other parameters of the model. This is necessary to handle more complex models, which became essential for detailed analysis of the samples, because the amount of independently varied parameters otherwise quickly increases and the runtime of the programm consequently exceeds manageable limits. Also, some parameters are coupled to each other by nature, for example the bottom roughness of a layer with the top roughness of the subjacent layer, if no interface is present between these layers. Without parameter coupling, it is not possible to take such phenomena into account with acceptable effort.

3.4 iXRR - an X-ray reflectivity analysis tool

iXRR is a GUI based simulation tool for X-ray reflectivity (XRR), which is based on the above introduced *RodsNPlots* and was developed and improved in our workgroup in the context of this thesis. The program was used for the analysis of XRR data in [41, 42, 43, 45] among others.

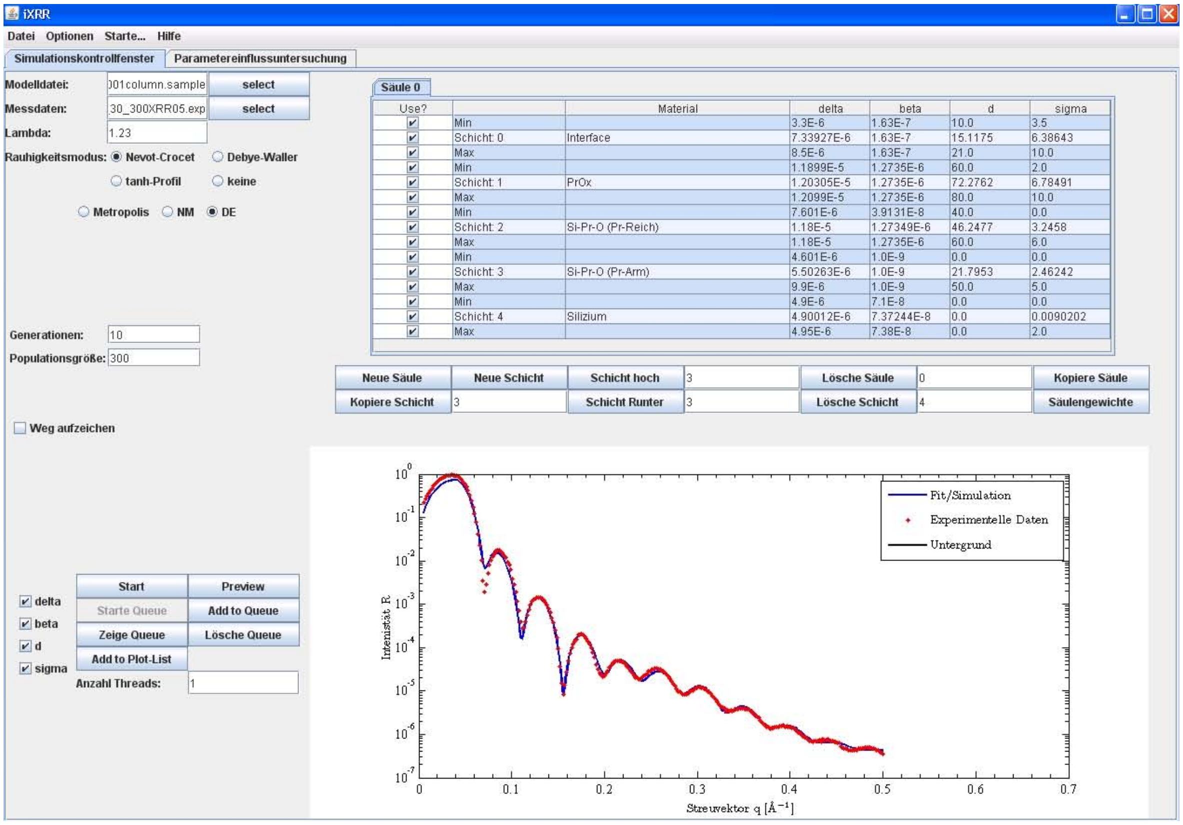
iXRR
Datei
Optionen
Starte...
Hilfe
Simulationskontrollfenster
Parametereinflussuntersuchung
select
select
Säule 0
Neue Säule
Neue Schicht
Schicht hoch
Lösche Säule
Kopiere Säule
Kopiere Schicht
Schicht Runter
Lösche Schicht
Säulengewichte
Start
Preview
Starte Queue
Add to Queue
Zeige Queue
Lösche Queue
Add to Plot-List
10^0
10^{-1}
10^{-2}
10^{-3}
10^{-4}
10^{-5}
10^{-6}
10^{-7}
Intensität R
0
0.1
0.2
0.3
0.4
0.5
0.6
0.7
Streuvektor q [Å^{-1}]
Fit/Simulation
Experimentelle Daten
Untergrund

Modelldatei: 001column.sample
Messdaten: 30_300XRR05.exp
Lambda: 1.23
Rauhigkeitsmodus: ● Nevot-Crocet ○ Debye-Waller ○ tanh-Profil ○ keine
○ Metropolis ○ NM ● DE
Generationen: 10
Populationsgröße: 300
☐ Weg aufzeichen
☑ delta
☑ beta
☑ d
☑ sigma
Anzahl Threads: 1

Use?		Material	delta	beta	d	sigma
☑	Min		3.3E-6	1.63E-7	10.0	3.5
☑	Schicht: 0	Interface	7.33927E-6	1.63E-7	15.1175	6.38643
☑	Max		8.5E-6	1.63E-7	21.0	10.0
☑	Min		1.1899E-5	1.2735E-6	60.0	2.0
☑	Schicht: 1	PrOx	1.20305E-5	1.2735E-6	72.2762	6.78491
☑	Max		1.2099E-5	1.2735E-6	80.0	10.0
☑	Min		7.601E-6	3.9131E-8	40.0	0.0
☑	Schicht: 2	Si-Pr-O (Pr-Reich)	1.18E-5	1.27349E-6	46.2477	3.2458
☑	Max		1.18E-5	1.2735E-6	60.0	6.0
☑	Min		4.601E-6	1.0E-9	0.0	0.0
☑	Schicht: 3	Si-Pr-O (Pr-Arm)	5.50263E-6	1.0E-9	21.7953	2.46242
☑	Max		9.9E-6	1.0E-9	50.0	5.0
☑	Min		4.9E-6	7.1E-8	0.0	0.0
☑	Schicht: 4	Silizium	4.90012E-6	7.37244E-8	0.0	0.0090202
☑	Max		4.95E-6	7.38E-8	0.0	2.0

Schicht hoch: 3
Lösche Säule: 0
Kopiere Schicht: 3
Schicht Runter: 3
Lösche Schicht: 4

Figure 3.6: *iXRR* screenshot. The top right area defines the model, the top left area sets the fitting algorithm. At the bottom, measured data (red dots) is compared to the calculated intensity distribution (blue line) according to the model above.

iXRR was developed in [11]. The GUI is based on the *RodsNPlots* GUI and the possible models to describe a sample are comparable to the ones of *RodsNPlots* in terms of complexity. The calculations are based on the theoretical description in chapter 2.2. The actual fitting parameters for each layer are the refractive index (more precisely *delta* and *beta*, cf. chapter 2.2), the layer thickness, and the interface roughness at the top of this layer.

As with *RodsNPlots*, it is possible to use *multi column models* to simulate laterally coexisting species with *iXRR*, too. For practical purposes, however, it is problematic to produce reliable *multi column models*, at least for the samples investigated in this work. The reason is that the intensity contribution of the respective columns cannot be separated clearly. This is in contrast to the analysis of X-ray *diffraction* data, where the Bragg positions originating from the respective columns are often delocalized, which simplifies the analysis significantly.

Regardless of this problem, XRR data analysis of praseodymium oxide on Si(111) by use of *iXRR* is usually of high accuracy. This is because the different columns are almost indistinguishable regarding their properties that are relevant for XRR. The refractive index for X-rays basically depends on the electron density of the material, which is nearly identical for different oxidation stages of PrO_x. Two columns with different interface roughnesses can be approximated very well by one column taking the weighted average of the respective roughnesses. And the remaining fitting parameter, the layer thickness, is again almost identical for different columns. Consequently, single column models yield good results for the analysis of the samples presented in this work and are therefore used in the following XRR results.

Original publication Applied Physics Letters **93**, 032905 (2008)
available at `http://dx.doi.org/10.1063/1.2958227`

Epitaxy of Single Crystalline PrO_2 films on Si(111)

T. Weisemoeller*, C. Deiter*, F. Bertram*, S. Gevers*,
A. Giussani**, P. Zaumseil**, T. Schroeder**, J. Wollschläger*,[6]

* *Department of Physics, University of Osnabrück, Barbarastrasse 7, D-49069 Osnabrück, Germany*
** *IHP, Im Technologiepark 25, 15236 Frankfurt (Oder), Germany*

---

[6] Electronic mail: joachim.wollschlaeger@uos.de

Original publication Journal of Applied Physics **105**, 124108 (2009)
available at `http://dx.doi.org/10.1063/1.3152796`

Post deposition annealing induced transition from hexagonal Pr_2O_3 to cubic PrO_2 films on Si(111)

T. Weisemoeller*, F. Bertram*, S. Gevers*, A. Greuling, C. Deiter*,
H. Tobergte*, M. Neumann*, A. Giussani**, T. Schroeder**, J. Wollschläger*,[7]

* *Department of Physics, University of Osnabrück, Barbarastrasse 7, D-49069 Osnabrück, Germany*
** *IHP, Im Technologiepark 25, 15236 Frankfurt (Oder), Germany*

---

[7] Electronic mail: joachim.wollschlaeger@uos.de

Original publication Physical Review B **79**, 245422 (2009)
available at `http://dx.doi.org/10.1103/PhysRevB.79.245422`

Effect of amorphous interface layers on crystalline thin film X-ray diffraction

T. Weisemoeller, F. Bertram, S. Gevers, C. Deiter, A. Greuling, J. Wollschläger[8]

Department of Physics, University of Osnabrück, Barbarastrasse 7, D-49069 Osnabrück, Germany

---

[8] Electronic mail: joachim.wollschlaeger@uos.de

7 Further results on thin praseodymia films on Si(111)

This section contains results that have not been published in scientific journals, presently. However, these results are of importance for X-ray structure analysis (with *RodsNPlots*) in general and of course of special interest for the analysis of praseodymium oxide (on Si(111)). Furthermore, results for bulk praseodymium oxide are connected to thin film preparation of praseodymium oxide. While this may seem an obvious approach, it has not been done in an adequate way, until now.

7.1 Simulations of oxygen vacancies with RodsNPlots

In previous chapters, the occurrence of oxygen vacancies in $PrO_{2-\delta}$ films was discussed. The additional peak at $L = 1.5$, which is shown in [41], can be explained by the model given in [41]. Because the peak is only observed in vertical direction and *not* in lateral direction, oxygen vacancies are assumed to be ordered only in vertical direction.

In [44], simulations with RodsNPlots were done to verify the model and/or to get further information about the structure of $PrO_{2-\delta}$ films on Si(111). For this purpose, a modified PrO_2 unit cell was implemented. It consists of two PrO_2 unit cells on top of each other, with a single oxygen atom missing at the top of the upper PrO_2 cell. The doubled vertical unit cell size implies twice as many Bragg peaks on a CTR, following the Laue equation 2.60. However, every second peak is symmetry forbidden, so that $2N$ PrO_2 cells should consequently yield an identical diffraction pattern compared to N doubled PrO_2 cells.

The missing oxygen atom in every second unit cell softens this forbiddenness, so that every second Bragg peak is no longer completely forbidden but rather much weaker than the remaining Bragg peaks. These superstructure peaks are exemplary shown in Fig. 7.1.

The simulation of actual thin film structures or substrates, however, is problematic, because the calculation of the roughness (cf. chapter 2.3) implies that damping effects due to roughness are maximized between Bragg positions: Eq. 2.74 approximates the damping effect by (periodic) cosine functions, so that the amplitude of a wave diffracted at a thin film is

$$A(\boldsymbol{q}) = A_0\, C\, F(\boldsymbol{q})\, \frac{e^{-\sigma_-^2\,(1-\cos \boldsymbol{q}\cdot\boldsymbol{c})} - e^{i\,\overline{N_3}\,\boldsymbol{q}\cdot\boldsymbol{c}} \cdot e^{-\sigma_+^2\,(1-\cos \boldsymbol{q}\cdot\boldsymbol{c})}}{1 - e^{i\,\boldsymbol{q}\cdot\boldsymbol{c}}}\ . \tag{7.1}$$

The roughness terms

$$e^{-\sigma_-^2\,(1-\cos \boldsymbol{q}\cdot\boldsymbol{c})} \qquad \text{and} \tag{7.2}$$

$$e^{-\sigma_+^2\,(1-\cos \boldsymbol{q}\cdot\boldsymbol{c})} \tag{7.3}$$

have no influence if

$$(1-\cos \boldsymbol{q}\cdot\boldsymbol{c}) = 0\ , \tag{7.4}$$

which is equivalent to

$$\boldsymbol{q}\cdot\boldsymbol{c} = 2\pi\, l \tag{7.5}$$

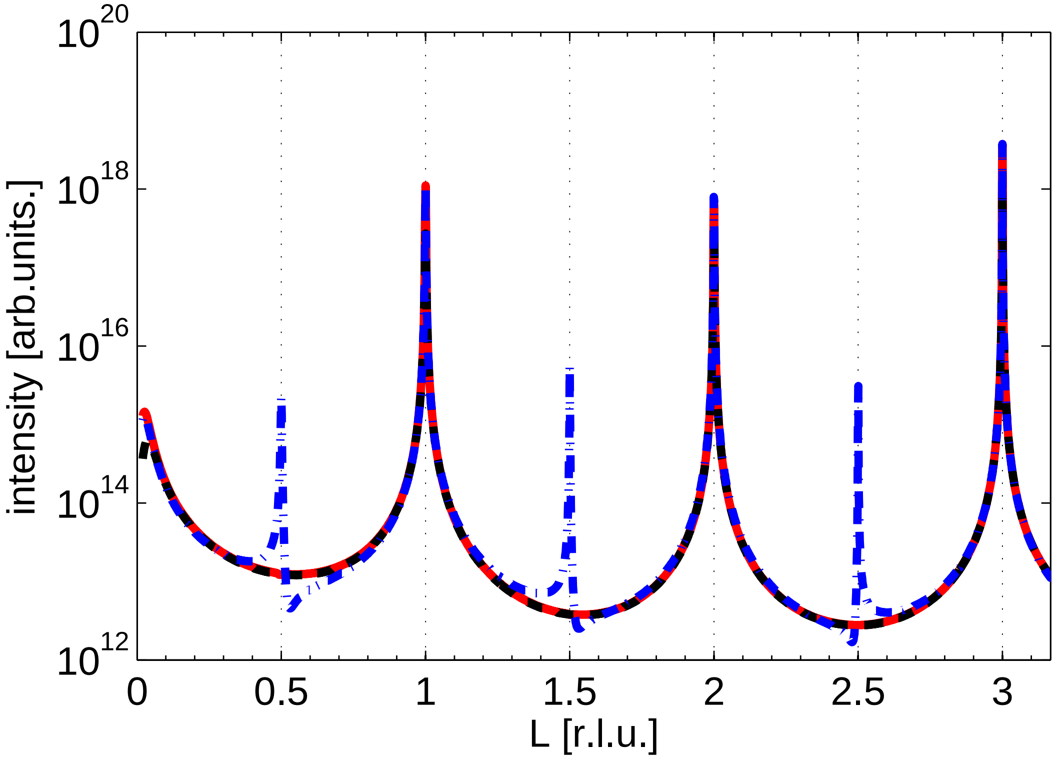

Figure 7.1: Simulation of a PrO_2 substrate with an oxygen atom missing in every second unit cell(vertically) and without roughness (blue dash-dotted line). Compared to PrO_2 without oxygen vacancies, additional Bragg peaks at $L = \frac{2N+1}{2}$ with $N \in \mathbb{N}$ occur due to the larger unit cell. A *non doubled* PrO_2 unit cell (black line) correctly shows the same intensity distribution as the *doubled* PrO_2 unit cell (red dashed line). Reciprocal lattice units (r.l.u.) are chosen with respect to the *non* doubled PrO_2 unit cell.

with $l \in \mathbb{N}$. The problem is that a doubled unit cell (superstructure), like the one of the two PrO_2 unit cells on top of each other, halves the periodicity of the cosine function as $\boldsymbol{c}$ is doubled (compared to the single PrO_2 unit cell), so that the roughness does not damp the intensity at $L = \frac{2N+1}{2}$ with $N \in \mathbb{N}$. This is of course wrong as a formal doubling of the unit cell does not imply any changes in the actual crystal structure and should hence not change the results of the simulation. The results of the simulations for praseodymia substrates with roughness are presented in Fig. 7.2

For reasons of simplicity, these effects are presented for substrates, which are treated as semi-infinite crystals (cf. chapter 2.3.7). Nevertheless, the same effects are also observable for thin films. As actual samples show significant roughness, a decent fit to measured data is not possible for the data parts which are significantly influenced by oxygen vacancies. Even so, the above simulations show that oxygen vacancies can explain the observed additional peaks. Not only are the positions of the additional peaks as expected, but the intensity is also reasonable. Both simulated and measured data show the intensity is approximately 1%

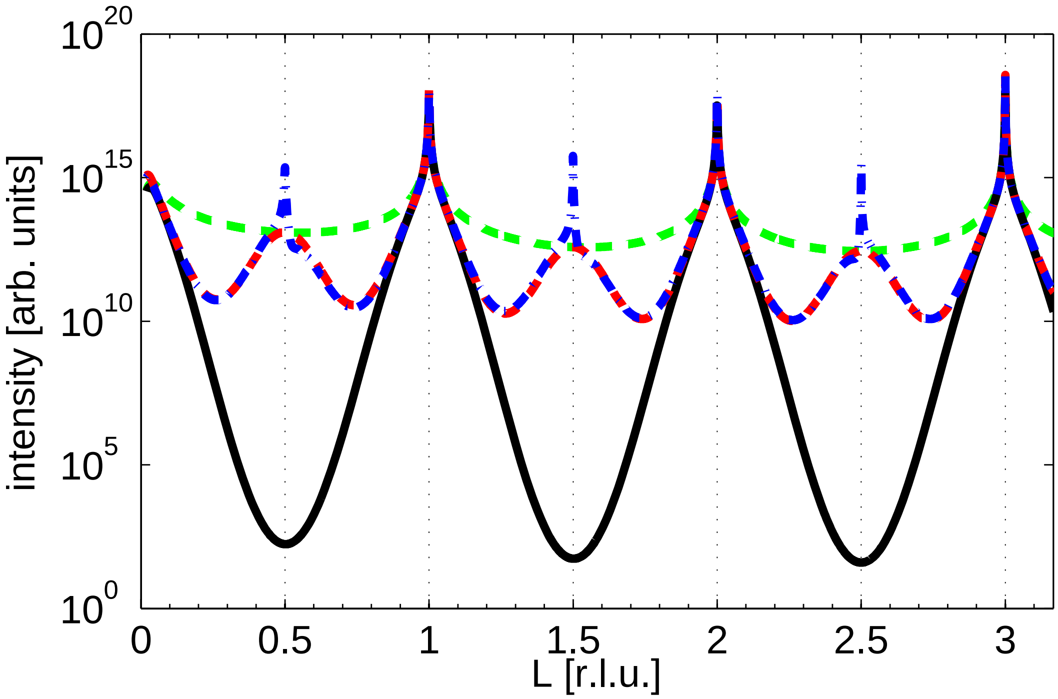

Figure 7.2: Simulation of different PrO_2 substrates *with* surface roughness. The substrate consisting of single PrO_2 unit cells (black line) is calculated correctly. The substrates of doubled PrO_2 unit cells *with* oxygen vacancies (blue dash-dotted line) and *without* (red dashed line) oxygen vacancies incorrectly show a broad peak at $L = \frac{2N+1}{2}$ with $N \in \mathbb{N}$. Comparison with the PrO_2 substrate without roughness (dashed green line, identical to the black line from Fig. 7.1) confirms that at $L = \frac{2N+1}{2}$ with $N \in \mathbb{N}$, damping shows no effect for the doubled unit cells. Furthermore, the blue dash-dotted line for the substrate with oxygen vacancies correctly shows peaks at $L = \frac{2N+1}{2}$ with $N \in \mathbb{N}$ due to the oxygen superstructure.

of the intensity of the PrO_2 Bragg peaks.

Albeit, a quantitative analysis of the number of oxygen vacancies, which would be very interesting with respect to the results discussed in the above chapters, seems to be too far fetched. An upper limit cannot be given because it is not known to what percentage oxygen vacancies are ordered or unordered. A lower limit cannot be given because the influence of the missing oxygen atom on the positions of the remaining atoms is not known. In the current model, no such influence is implemented. That means that at half integer positions, the amplitude originating from the praseodymium atoms is zero (due to destructive interference) in our simulations. This is obviously not correct as the positions of the neighboring atoms are definitely influenced by the missing of the oxygen atom. As scattering of the X-ray photons is much more probable at the heavy praseodymium atoms compared to scattering at oxygen atoms, a small shift in praseodymium position may have significant influence on the intensity of the superstructure peak.

For thin films, the superstructure peak shifts slightly due to interference effects. This will be investigated in upcoming work. In principle, it is possible to assign this peak to one of the two coexisting praseodymia species. The related lattice constant can potentially be determined more correctly than from only fitting the double peak at $L = 2$ (cf. [41]). This of course also allows for a more precise determination of the remaining fit parameters. Beside that, it is also possible to determine which of the two praseodymia species contains ordered oxygen vacancies.

The problems associated with the roughness calculation currently used in the XRD model occur for calculations with large unit cells and superstructures in general. Hence, the model for surface roughness from chapter 2.3 has to be rethought.

7.2 On thin praseodymia films

7.2.1 Multi column models and thin films

Some solid state chemical reaction take place without a displacement of the atomic positions of one kind of atom of the structure. This is also the case for the oxidation and deoxidation of cubic or pseudocubic praseodymia species. The chemical transformations consequently occur without a great change in the framework of praseodymium atoms. The only exception is general strain due to change of lattice constants during the (de-)oxidation. Hence, the position of the praseodymium atoms in the lattice is unchanged, whereas the extremely mobile oxygen atoms are subjected to a diffusion process [46]. This supports the phase transition model proposed in [42], where the praseodymium atoms are only displaced minimally during the phase transition from hexagonal Pr_2O_3 to cubic PrO_2.

Boulesteix and Eyring furthermore showed that several praseodymia species can be considered as PrO_2 with ordered oxygen vacancies. In Pr_7O_{12}, for example, these vacancies are ordered along parallel strings in [111] direction. The still fluorite-like structure is slightly distorted and can be looked at as slabs of Pr_7O_{12} composition containing $\{135\}$ planes of six-coordinated praseodymium layers with adjacent seven-coordinated praseodymium layers [46]. Pr_9O_{16} contains additional PrO_2 slabs that grow coherently across these $\{135\}$ planes.

The praseodymium atoms are hence differently coordinated. Their ion radius and therefore their distance to each other is consequently different and strain due to buckling occurs because the lattice constant of the underlying fluorite lattice is slightly different. Nevertheless, interfaces between different oxide species in bulk crystals are well defined in one direction. A phase transformation of similar praseodymia species was found to start with the growth of a needle-like domain [46]. During such a phase transformation, praseodymium oxide thus has to viewed as a mix of two coexisting praseodymium oxide species. Rudenko and Boganov state that this coexistence is the rule rather than the exception, so that praseodymium oxide rarely consists of only one species [29].

Lowe *et al.* point out that larger domains of one species result in smaller interfacial effects and thus less strain between the two species [47]. This reinforces the multi column model introduced in [42]. The oxygen vacancies in a $PrO_{2-\delta}$ film are not distributed evenly across the film. Instead, parts of the film are converted to PrO_2, while other parts contain oxygen vacancies. The ordering of these oxygen vacancies can be different from the ordering in the known praseodymium oxide phases because of the significant strain in the thin films investigated in this work. However, the principle that strain effects between the species in a film must be minimized (because this is energetically favorable) leads to relatively large single crystalline parts of the film, with the interfaces between those species perpendicular to the surface. This is exactly what the multi column model describes.

Also important to note is that phase transitions in praseodymium oxide powders must consequently start at the surface of a crystal because this way stress will be minimized [47]. While this is obviously true for powder praseodymia, thin films have to be discussed separately. This is because the lateral lattice distance might be fixed. For the samples investigated in this thesis, the in plane lattice constant is fixed to the value of hexagonal praseodymium oxide. In these cases, only slight additional stress will consequently occur at the (relatively short) cubic to hexagonal boundary. This influence can therefore be expected to be smaller compared to powder data. Therefore, it is uncertain whether a phase transformation in thin films starts at the top or at the bottom of the film.

[42] shows that for a phase transition from hexagonal to cubic structure, no shift of the two lowest praseodymium layers has to occur if the transition is to a *B-type* cubic structure. This is not the case if the transition is to an *A-type* cubic structure. As noted above, hexagonal films that are transformed to a cubic structure by annealing in oxygen are indeed *B-type*. This indicates that the transformation might start at the bottom of the oxide layer. However, further investigations are necessary to obtain clear results in this regard.

Lowe *et al.* furthermore state that they investigated larger crystals of an average size of 0.5 to 1.0 μm and state that this is five to ten times the size of praseodymium oxide powder particles. Therefore, we assume that the particle size in powder praseodymia investigated in that work is approximately 100 nm. Lowe *et al.* point out that the length of the diffusion path for oxygen in the particles plays an important role. Larger crystals lead to a delay of the (de-)oxidation process, so that more time is needed to reach equilibrium. Because of that, the hysteresis is also larger. The thickness of the films investigated in this thesis is only 5 nm. This does probably cause the (de-)oxidation process to happen significantly faster than for powder praseodymia.

Which equilibrium oxygen content is reached (after sufficient time), however, is not influenced by the crystal size. Nevertheless, data for powder praseodymia cannot be expected to be identical for thin films. This is because strain effects energetically favor certain oxidation stages PrO_x over others. While the strength of this influence is still unclear, the direction of the influence *is* clear. [42] shows that the lateral lattice constants of praseodymia films that were transformed to a cubic structure are still the lattice constant of hexagonal Pr_2O_3. This value is very close to the lateral lattice constant of $PrO_{1.833}$, while the difference to PrO_2 is relatively large and the one to cubic Pr_2O_3 is even larger. Therefore, we assume that compared to the situation for powder praseodymia, thin films with cubic structure tend to the $PrO_{1.833}$ oxidation stage, because in this case strain is minimized. This will also be discussed in chapter 7.2.3 and chapter 7.2.4.

7.2.2 Hydroxides

Hexagonal Pr_2O_3 is particularly unstable if exposed to water and consequently tends to form hydroxides if exposed to non-dry air [48]. As the films investigated in this thesis were grown in the hexagonal form and converted to films of cubic structure only *after* they were exposed to air, it cannot be excluded that hydroxides were formed. Haschke and Eyring showed that hydroxides ($Pr(OH)_3$) and nitrates ($Pr(OH)_2NO_3$ and $Pr_2(OH)_5NO_3$) are reduced to praseodymium oxide if annealed to approximately 400°C, while hydroxycarbonates ($PrOHCO_3$) is only reduced to Pr_2O_3 very slowly even at temperatures of up to 800°C.

Kang and Eyring measured X-ray powder diffraction patterns of PrO_2 and mixtures of PrO_2 and praseodymium hydroxide [49]. Additional peaks close the $(111)_{bulk}$ peak of PrO_2 emerge due to the $Pr(OH)_3$ contamination. These peaks appear mostly at slightly smaller scattering vectors than the PrO_2 peak, but are generally present all around the $(111)_{bulk}$ peak.

This makes hydroxide contaminations hard to detect in the specular scans discussed in the previous chapters. However, [42] shows an unexpected peak at $L \approx 0.93$ on the specular rod for the praseodymium oxide on Si sample which was post deposition annealed at only 300°C. In contrast to PrO_x peaks, this peak does not appear at the related position close to the $(222)_{bulk}$ peak of PrO_2. Therefore, it is either caused by a praseodymium oxide species with a very large unit cell and lots of point defects or by hydroxides. As no appropriate peak for the large praseodymium oxide species appears on the $(01L)_{bulk}$ rod shown in [42] appears, we assume that hydroxides are present on this sample.

As no such peak appears for samples annealed at higher temperatures, we assume that hydroxides are removed from thin films of praseodymium oxide by post deposition annealing at 400°C or more in 1 atm. oxygen for 30 minutes. This is in line with the results for powder praseodymium oxide [49].

7.2.3 On the Pr_2O_3 region

If praseodymium oxide is evaporated under UHV conditions, it crystallizes as hexagonal Pr_2O_3 on clean Si(111) surfaces. Liu *et al.* [50] reported that these thin films of hexagonal Pr_2O_3 are transformed to cubic Pr_2O_3 by post deposition annealing in 1 atm. nitrogen and speculated that nitrogen triggers the phase transition. Schroeder *et al.* [33] observed that the phase transition also occurs if the annealing process takes place in 10^{-5} mbar (nitrogen-free) oxygen atmosphere. They also noticed that an amorphous interface is formed between substrate and oxide film during the post deposition annealing process and therefore attributed the phase transition to a disconnection of film and substrate due to the interface formation.

In the above chapters, it was shown that the lateral lattice constant of thin films transformed to cubic PrO_2 is the same as in hexagonal bulk Pr_2O_3. We therefore assume that the lateral lattice constant of thin praseodymia films does not change significantly during the phase transformation induced by post deposition annealing in oxygen. This assumption is reinforced by the results from Zaumseil [51], who investigated a Si(111)/c-Pr_2O_3/Ge crystalline system and observed that the Pr_2O_3 layer is strained.

Actually, the lateral lattice constant determined by Zaumseil is again very close to the one of the originally deposited hexagonal Pr_2O_3 film (lattice mismatch of 0.6%), although the lateral lattice mismatch between bulk h-Pr_2O_3 and bulk c-Pr_2O_3 is rather large (lattice mismatch of 2.1%).

Hence, it is improbable that the phase transition is due to a disconnection of film and substrate. Once again, the answer to the problem comes from data for bulk praseodymium oxide. Rudenko and Boganov [29] showed that stoichiometric Pr_2O_3 is energetically favorable in the *hexagonal* lattice. However, if the oxygen content increases only slightly, this is no longer the case and the *cubic* lattice is energetically favorable. They consequently refer to the latter form as c-$Pr_2O_{3+\delta}$. The fact that hexagonal Pr_2O_3 has no room for additional oxygen atoms whereas cubic Pr_2O_3 has oxygen vacancies supports this thesis. Complementary, Turcotte *et al.* [52] believe that hexagonal Pr_2O_3 is not only the high temperature phase, but also the true low composition boundary over the complete temperature axis. However, it can only be obtained by heating praseodymium oxide in extremely low oxygen partial pressure environment and was thus often found to coexist with c-Pr_2O_3.

Evaporation of the thin films investigated in this work takes place under UHV conditions. This might be the reason why the films crystallize in the hexagonal form. Furthermore, lattice matching on Si(111) is better for hexagonal than for cubic Pr_2O_3. In addition, excess oxygen might also form Si-O bonds.

Transformation to cubic Pr_2O_3 is achieved by annealing in low pressure oxygen. In our opinion, this annealing process simply increases the oxygen content of the film, so that $Pr_2O_{3+\delta}$ is formed, which is energetically unfavorable in the hexagonal form and is therefore converted to the cubic structure. Because Si is very reactive to oxygen, this higher oxygen content accompanies the formation of an SiO_2 rich interface layer. We assume that the formation of the interface layer starts before the phase transition, as TEM images showed an interface layer for all films transformed to the cubic structure. In this case, the interfacial layer acts as a diffusion barrier for oxygen. If this barrier is strong enough, the oxygen content in the film increases sufficiently to induce the phase transition. However, it is also possible that the phase transformation starts before the formation of an interfacial layer. This may also depend on different parameters during the annealing process.

If cubic films are annealed in oxygen at temperatures above 500°C, not only an SiO_2 rich interface layer, but also an additional Pr rich interface layer is formed (cf. [42]). This layer is located between the SiO_2 rich interface layer and the oxide film and its formation is attributed to either Si or Pr diffusion. Because the lateral lattice constant of the film is fixed, as noted above, it seems improbable that Pr diffusion takes place. Furthermore, it is interesting that the films were deposited at a substrate temperature of 625°C, which is significantly higher than the temperature at which the formation of the Pr-rich interfacial layer starts. Nevertheless, Schroeder *et al.* [33] report that the hexagonal films and the Si substrate form an atomically sharp interface. Hence, no diffusion of Si atoms takes place during the deposition of the film at 625°C.

We assume that Si diffusion does therefore only take place from SiO_2 and not from crystalline Si. As a result, the formation of the SiO_2 rich interface might be a precondition for the formation of the Pr-rich interface, so that prevention of the former might hinder the formation of the latter interface. Passivation of the Si surface could consequently enhance thermal stability of the interface significantly. Experiments with highly boron-doped Si surfaces are currently under progress in our workgroup.

As a side note, c-Pr_2O_3 is hard to distinguish from other praseodymia species with slightly higher oxygen content in thin films. Although exact numbers for the determined vertical lattice constant are not given in [33], it is obvious that the peak position of the $\theta - 2\theta$ scan is rather close to the one of bulk c-Pr_2O_3 than to the one of *strained* c-Pr_2O_3. However, the film *is* strained, as can be seen from the respective in plane scans.

The c-Pr_2O_3 presented in [51], however, correctly shows the vertical lattice constant of the *strained* unit cell. The former film is prepared by post deposition annealing in 10^{-5} mbar oxygen. The latter film is prepared by annealing in 1 atm. oxygen and is thereafter reduced by the deposition of germanium on top. The germanium atoms form Ge-O bonds, which are evaporated. This way the film is reduced to Pr_2O_3.

From these observations, it seems like the latter film has a significantly bigger unit cell, which corresponds to less oxygen content. We therefore assume that the δ in the former film of c-$Pr_2O_{3+\delta}$ is significantly higher. Annealing in 10^{-5} mbar oxygen for 30 min hence seems to result in excess oxygen in the c-Pr_2O_3 film.

In our opinion, it is necessary to further investigate the respective equilibrium conditions of thin films of praseodymium oxide on Si(111). In situ XRD during the post deposition annealing process seems to be the method of choice, here.

7.2.4 On the PrO_2 region

The praseodymium oxide phase diagram (cf. Fig 2.18) shows that there is a miscibility gap between Pr_6O_{11} ($PrO_{1.833}$) and PrO_2 at room temperature. Hyde *et al.* reported that if powder $PrO_{1.833}$ is annealed at oxygen partial pressures of close to 1 atm., further oxidation to the dioxide begins. This effect is reversed when a temperature of approximately 335°C is reached [53]. Hyde *et al.* also state that rapid equilibration within a few minutes takes place at temperatures of 400°C and above. At lower temperatures, the (de-)oxidation process tends to become very slow. Oxidation from $PrO_{1.833}$ to $PrO_{1.95}$ at 1 atm. oxygen and 286°C, for example, takes 1000 minutes. Further oxidation to $PrO_{1.99}$ takes another 1000 minutes [30]. Although oxidation of thin films of 5 nm might happen faster than the oxidation of powder (approximately 100 nm particle size), these are annealing times that seem to be undesirable.

MacChesney *et al.* showed pressure-temperature relations for the higher praseodymium oxides in [54]. The results are graphically shown in Fig. 7.3. Depending on temperature and oxygen partial pressure, the equilibrium stoichiometry is either PrO_2 (upper left of the black dividing line) or Pr_6O_{11} (lower right of the black dividing line). Lower oxides are not discussed here and are therefore not included in the Figure.

It is important to understand that at low temperatures, the (de-)oxidation process is so slow that the system effectively freezes out and the stoichiometry remains unchanged. It is well known that Pr_6O_{11} is prepared by annealing praseodymium oxide in air and subsequently cooling the powder down slowly. Following the red dash-dotted line in Fig. 7.3, for temperatures below 260°C, PrO_2 is the equilibrium stoichiometry in air (0.2 atm. oxygen partial

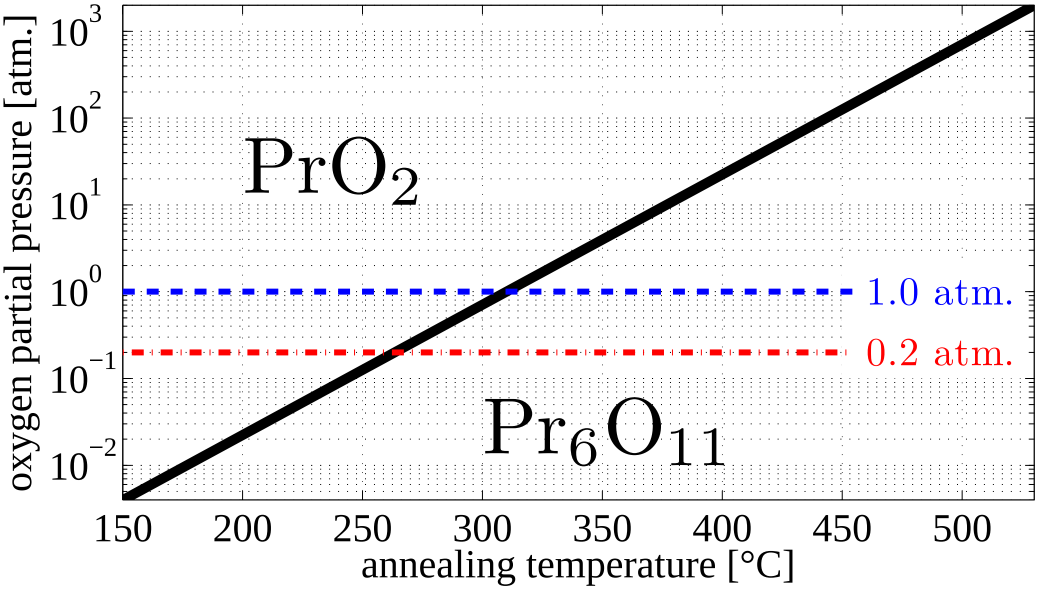

Figure 7.3: Pressure temperature relations for the higher praseodymium oxides, data taken from [54]. Depending on temperature and oxygen partial pressure, the equilibrium stoichiometry is either PrO_2 (upper left of the black dividing line) or Pr_6O_{11} (lower right of the black dividing line). The blue dashed line marks the pressure used for post deposition annealing of the samples prepared in the context of this thesis. The red dash-dotted line marks the partial pressure of air. It is important to note that these are *equilibrium* stoichiometries. The (de-)oxidation process slows down significantly at lower temperatures.

pressure). This shows that at such temperatures, the powder has already frozen out. This is in line with the above mentioned results from [30], where the oxidation process (in 1 atm. oxygen to produce PrO_2) was extremely slow at 286°C.

Powder PrO_2 in [54] was prepared by annealing in 225 atm. oxygen at 351°C for 68 hours. The system was thereafter quenched to room temperature and only then the pressure was released.

In [29], PrO_2 was prepared by annealing in only 1 atm. oxygen. In this environment, the powder was cooled from 500°C to 400°C very slowly (20°C/hour) and even slower down to 200°C.

These approaches seem appropriate, based on the data shown in Fig. 7.3. The samples investigated in this work, in contrast, were post deposition annealed in 1 atm. oxygen at different temperatures from 100°C to 700°C for 30 minutes. The films annealed at 100°C and 200°C were not converted from hexagonal to cubic structure. This is in line with results for powder, because the films are still frozen out at these temperatures.

At higher temperatures of 300+°C, oxidation took place. This is again in line with powder results. [41] shows that all of these films have two coexisting vertical lattice constants and hence two coexisting stoichiometries. However, no further structural differences were observed, apart from a small superstructure peak in vertical direction. This is because all higher oxides of PrO_x share the same Pr cation lattice, as illustrated in [55]. These structures are hard to distinguish because the main difference lies in the position of oxygen vacancies. For powder, the calculated shifts of the Pr ions are unlikely to be modeled correctly because the sheer amount of variables makes it possible to obtain any desired result without the shifted positions necessarily being correct [55]. Also, thin films might behave differently due to the significant strain effects. Therefore, the oxygen content of the films is in our opinion best determinable via the unit cell size.

Based on these assumptions, the oxygen content of the films increased with annealing temperature. This may at first sight seem to contradict the data shown in Fig. 7.3. After all, rapid equilibration within a few minutes takes place at temperatures of 400°C and above for powder praseodymia [30]. It is not reasonable to suspect that thin films need higher temperatures for rapid equilibration as they are much thinner than powder particles. Temperatures of 400+°C correspond to Pr_6O_{11} equilibria at 1 atm. oxygen.

The reason why the samples annealed at higher temperatures contain higher oxides is in our opinion the different cooling process. The phase transition from Pr_6O_{11} to PrO_2 should start at 310°C, based on powder data shown in Fig. 7.3. As in thin films on Si(111), PrO_2 is more strained than Pr_6O_{11}, the black dividing line in Fig. 7.3 might even shift slightly to the left, so that the phase transition starts at even lower temperatures (or higher oxygen partial pressures). However, the final oxidation happens when the sample is cooled down. If the sample holder was heated to higher temperatures, this delays the cooling of the sample because the holder acts as a heat reservoir. We assume that this is the determining factor that causes the higher final oxidation of the samples annealed at higher temperatures.

Regardless of that, either very slow cooling or higher oxygen partial pressures are needed to produce PrO_2 films without oxygen vacancies. To us, the latter seems to be a much more promising approach because extremely long post deposition annealing times might inflate the amorphous interface layer and lead to more point defects in the sample.

8 Summary and Outlook

This chapter provides a brief summary of the most important results presented above and also discusses the next research steps in this context.

In this thesis, it was shown that hexagonal h-Pr_2O_3 can be transformed to B-oriented twin free films of c-PrO_2 with oxygen vacancies by post deposition annealing in 1 atm. oxygen at temperatures from 300°C up to 700°C for 30 minutes. Films annealed at 100°C and 200°C are still purely hexagonal Pr_2O_3 after the annealing process. In the *transformed* films, two stoichiometric phases coexist laterally. The *lateral* lattice constant of both species is almost identical to the one of the originally deposited h-Pr_2O_3. Therefore, we assume that the lateral lattice constant is pinned throughout the oxidation process.

The species are hence strained and show different *vertical* lattice constants, depending on the amount of oxygen vacancies. In some samples, those vacancies were partly ordered vertically, leading to a unit cell twice as large as expected for stoichiometric PrO_2.

During the annealing process, an amorphous interfacial layer between substrate and oxide was detected. While the existence of this layer was known before, it was possible for the first time to quantify the thickness of the praseodymium rich part of this interface for epitaxially grown films. It was shown that this layer starts to grow significantly only during post deposition annealing at 500°C or more.

These and other results for thin films were connected to previously published data for *bulk* praseodymia. The multi column model mentioned above for laterally coexisting praseodymia species in thin films was backed up by powder data. As a matter of fact, it was shown that this coexistence of several praseodymia species can be expected to be the rule rather than the exception.

Strong evidence was found that results interpreted previously as stoichiometric cubic Pr_2O_3 contain more oxygen than originally thought. It was shown that the phase transition from hexagonal to cubic praseodymium oxide cannot rely mainly on a disconnection between film and substrate, as it was thought before. Instead, the driving force behind this phase transition is originated in the film itself. Even post deposition annealing in 10^{-5} mbar oxygen raises the oxygen content of the film sufficiently to favor the cubic structure over the hexagonal structure, because the latter is not able to incorporate the additional oxygen atoms of the $Pr_2O_{3+\delta}$ stoichiometry, which is (strictly speaking) generated by the post deposition annealing process.

Beside that, it was indicated that the formation of the praseodymium rich part of the interface is connected to the formation of the SiO_2 rich part of the interface, so that suppression of the growth of the latter can be expected to prevent or at least to slow down growth of the former part of the interface.

Finally, based on the results for powder praseodymium oxide, it was demonstrated that the formation of thin praseodymium dioxide films on Si(111) *without* oxygen vacancies is unlikely to be successful by annealing without increasing oxygen partial pressure significantly.

As a (meaningful) byproduct, a new X-ray diffraction analysis method was introduced. The new method makes it possible to investigate amorphous structures located between crystalline structures in multi layer systems under the assumption that significant interference between the waves diffracted at the different crystalline layers occurs. This is obviously the case for many epitaxially grown films with amorphous interface layers, as the lattice constants are related.

The outlook for further investigations following the results presented here consequently includes the application of this new analysis method on previously recorded and future data from X-ray diffraction.

Furthermore, the (de-)oxidation process of praseodymia films of different thickness have to be investigated. The results for powder praseodymia lead the way here, but small differences due to strain effects and the limited film thickness are to be expected. Because it can no longer be assumed that films and substrate are disconnected from each other after the annealing process, it might also be possible to influence the lateral strain in a desired direction, for example by variation of the substrate temperature during deposition of the film. This is not only interesting because the lateral lattice constant itself can be influenced, but also because the strain is expected to influence equilibrium conditions for certain stoichiometries.

However, a prerequisite for decent analysis of these films is the preparation and exact characterization of those praseodymia films that represent the boundaries of the praseodymium oxide phase diagram, namely hexagonal Pr_2O_3 as well as *single phase stoichiometric* Pr_2O_3 and PrO_2. The importance of this cannot be overemphasized. In the past decades of powder praseodymia analysis, much confusion would have been avoided if proper preparation recipes would have been available from relatively early on.

We expect in situ X-ray diffraction and X-ray reflectivity measurements during post deposition annealing experiments to be the way to go, here. Beside a variance of oxygen partial pressure, temperature and duration, the use of oxygen plasma seems to be prosperous to increase the oxygen content of praseodymia films. It is important to note that during plasma treatment, it will be necessary to heat the sample to probably at least 300°C to allow proper oxygen transport within the oxide film. Also, heating to more than 400°C might be needed to clean the samples from hydroxides if the plasma treatment is done ex-situ.

In order to influence the interface formation, experiments with highly boron doped silicon surfaces are currently performed in our workgroup and yield promising results in terms of passivation of the Si surface before film deposition in order to prevent the formation of interfacial silicate.

A List of peer-reviewed publications

- M. Imlau , M. Fally, T. Weisemoeller, D. Schaniel
  Holographic light scattering in centrosymmetric sodium nitroprusside upon generation of light-induced metastable states
  Physical Review B **73**, 205113 (2006).
  available at `http://dx.doi.org/10.1103/PhysRevB.73.205113`

- D. Schaniel, M. Imlau, T. Weisemoeller, T. Woike, K.W. Kramer, H.U. Gudel
  Photoinduced nitrosyl linkage isomers uncover a variety of unconventional photorefractive media
  Advanced Materials **19**, 723 (2007).
  available at `http://dx.doi.org/10.1002/adma.200601378`

- A. Giussani, O. Seifarth, P. Rodenbach, H.J. Müssig, P. Zaumseil, T. Weisemoeller, C. Deiter, J. Wollschläger, P. Storck, T. Schroeder
  The influence of lattice oxygen on the initial growth behavior of heteroepitaxial Ge layers on single crystalline PrO_2*(111)/Si(111) support systems*
  Journal of Applied Physics **103**, 084110 (2008).
  available at `http://dx.doi.org/10.1063/1.2870270`

- T. Weisemoeller, C. Deiter, F. Bertram, S. Gevers, A. Giussani, P. Zaumseil, T. Schroeder, J. Wollschläger
  Epitaxy of single crystalline PrO_2 *films on Si(111)*
  Applied Physics Letters **93**, 032905 (2008).
  available at `http://dx.doi.org/10.1063/1.2958227`

- G. Jnawali, H. Hattab, C.A. Bobisch, A. Bernhart, E. Zubkov, C. Deiter, T. Weisemoeller, F. Bertram, J. Wollschläger, R. Möller, M. Horn-von Hoegen
  Epitaxial Growth of Bi(111) on Si(001)
  e-Journal of Surface Science and Nanotechnology **7**, 441 (2009).
  available at `http://dx.doi.org/10.1380/ejssnt.2009.441`

- S. Gevers, T. Weisemoeller, B. Zimmermann, F. Bertram, C Deiter, J. Wollschläger
  Structural phase transition of ultra thin PrO_2 *films on Si(111)*
  Journal of Physics: Condensed Matter **21**, 175408 (2009).
  available at `http://dx.doi.org/10.1088/0953-8984/21/17/175408`

- T. Weisemoeller, F. Bertram, S. Gevers, A. Greuling, C. Deiter, H. Tobergte, M. Neumann, A. Giussani, T. Schroeder, J. Wollschläger
  Post deposition annealing induced transition from hexagonal Pr_2O_3 *to cubic* PrO_2 *films on Si(111)*
  Journal of Applied Physics **105**, 124108 (2009).
  available at `http://dx.doi.org/10.1063/1.3152796`
- T. Weisemoeller, F. Bertram, S. Gevers, C. Deiter, A. Greuling, J. Wollschläger
  Effect of amorphous interface layers on crystalline thin film X-ray diffraction
  Physical Review B **79**, 245422 (2009).
  available at `http://dx.doi.org/10.1103/PhysRevB.79.245422`

Bibliography

[1] D.T. Bowron, G.A. Saunders, R.J. Newport, B.D. Rainford, and H.B. Senin. EXAFS studies of rare-earth metaphosphate glasses. *Phys. Rev. B*, 53(9):5268, 1996. `doi:10.1103/PhysRevB.53.5268`.

[2] J.R. Stetter, W.R. Penrose, and S. Yao. Sensors, Chemical Sensors, Electrochemical Sensors, and ECS. *Journal of The Electrochemical Society*, 150(2):11, 2003. `doi:10.1149/1.1539051`.

[3] R.D. Köhn, Z. Pan, J. Sun, and C. Liang. Ring-opening polymerization of $_D$, $_L$ -lactide with bis(trimethyl triazacyclohexane) praseodymium triflate. *Catal. Commun.*, 4(1):33, 2003. `doi:10.1016/S1566-7367(02)00244-3`.

[4] T. Schroeder, A. Giussani, J. Dabrowski, P. Zaumseil, H.-J. Müssig, O. Seifarth, and P. Storck. Engineered Si wafers: On the role of oxide heterostructures as buffers for the integration of alternative semiconductors. *Phys. Status Solidi C*, 6(3), 2009. `doi:10.1002/pssc.200880715`.

[5] G.K. Celler and S. Cristoloveanu. Frontiers of silicon-on-insulator. *J. Appl. Phys.*, 93(9):4955, 2003. `doi:10.1063/1.1558223`.

[6] Haruhiko Ono and Tooru Katsumata. Interfacial reactions between thin rare-earth-metal oxide films and si substrates. *Appl. Phys. Lett.*, 78(13):1832, 2001. `doi:10.1063/1.1357445`.

[7] Image source: wikipedia user Hmilch. Roentgen-Roehre.svg. `http://de.wikipedia.org/w/index.php?title=Datei:Roentgen-Roehre.svg&filetimestamp=20081223015047`, 14.04.2009.

[8] Image source: wikipedia user Cepheiden. Atom model for EDX DE.svg. `http://de.wikipedia.org/w/index.php?title=Datei:Atom_model_for_EDX_DE.svg&filetimestamp=20081114154844`, 14.04.2009.

[9] Image source: Copyright DESY/European XFEL. XFEL_Leuchtstaerke_EN.jpg. `http://www.xfel.eu/media/assets/XFEL_Leuchtstaerke_EN.jpg`, 15.04.2009.

[10] Image source: Bastian Holst. Undulator-prinzip.svg. `http://upload.wikimedia.org/wikipedia/de/3/38/Undulator-prinzip.svg`, 17.04.2009.

[11] F. Bertram. Röntgenreflektometrie an ultradünnen Schichten, 2007. Bachelor thesis.

[12] L. G. Parratt. Surface Studies of Solids by Total Refelection of X-Rays. *Physical Review*, 95(2):359, 1954.

[13] M. Tolan. *X-Ray Scattering from Soft-Matter Thin Films, Materials Science and Basic Research.* Springer, 1998.

[14] Image source: wikipedia user Matthias_M. Bragg.svg. `http://de.wikipedia.org/w/index.php?title=Datei:Bragg.svg&filetimestamp=20080402161705`, 08.05.2009.

[15] L. Névot and P. Croce. Charactization of surfaces by grazing x-ray reflection. Application to the study of polishing some silicate glasses. *Revue de Physique Appliquee*, 15(3):761, 1980.

[16] P. Beckmann and A. Spizzichino. *The scattering of electromagnetic waves from rough surfaces*. Norwood, MA, Artech House, Inc, 1987, 511 p., 1987.

[17] A. Greuling. Röntgenstrukturanalyse von Isolatorschichten, 2007. Master thesis.

[18] M. Hanke. Streuung von Röntgenstrahlen an selbstorganisierten Halbleiter-Inselstrukturen, 2002. PhD thesis. Available from: `http://www.cmat.uni-halle.de/publicationen/michael_hanke_dissertation.pdf`.

[19] F. Bertram. Röntgenstrukturanalyse von Oxidschichten, 2009. Master thesis.

[20] C. Deiter. Röntgenstrukturanalyse von Halbleiter-Isolator-Schichtsystemen, 2005. PhD thesis.

[21] K. Kopitzki and P. Herzog. *Einführung in die Festkörperphysik*. B.G. Teubner Stuttgart, 2002.

[22] M. Räkers. An x-ray spectroscopic study of novel materials for electronic applications, 2009. PhD thesis.

[23] K. Küpper. Electronic and magnetic properties of transition metal compounds: An x-ray spectroscopic study, 2005. PhD thesis.

[24] Image source: wikipedia user Ben Mills. Silicon-unit-cell-3D-balls.png. `http://upload.wikimedia.org/wikipedia/commons/f/f1/Silicon-unit-cell-3D-balls.png`, 24.05.2009.

[25] Z.C. Kang and L. Eyring. Proposal structure of $Pr_{88}O_{160}$ phase in binary, rare earth higher oxides. *Journal of Alloys and Compounds*, 408-412:1123, 2006. Proceedings of Rare Earths'04 in Nara, Japan. `doi:10.1016/j.jallcom.2004.12.186`.

[26] L. Eyring and N. C. Baenziger. On the Structure and Related Properties of the Oxides of Praseodymium. *J. Appl. Phys.*, 33(1):428, 1962. `doi:10.1063/1.1777136`.

[27] J. Zhang, R. B. Von Dreele, and L. Eyring. Structures in the Oxygen-Deficient Fluorite-Related R_nO_{2n-2} Homologous Series: $Pr_{12}O_{22}$. *J. Solid State Chem.*, 122:53, 1996. `doi:10.1006/jssc.1996.0081`.

[28] S. Gevers. SPA-LEED-Untersuchungen von Praseodymoxidschichten auf Si(111)-Substraten, 2007. Diplomarbeit.

[29] V. S. Rudenko and A. G. Boganov. Reduction cycle $MO_2 \rightarrow M_2O_3$ for cerium, praseodymium, and terium oxides. *Inorg. Mater. (USSR) (Engl. Transl.)*, 7:98, 1971.

---

[30] B. G. Hyde, D. J. M. Bevan, and L. Eyring. On the Praseodymium+Oxygen System. *Philosophical Transactions of the Royal Society of London. Series A, Mathematical and Physical Sciences*, 259(1106):583, 1966. `doi:10.1098/rsta.1966.0025`.

[31] T. Schroeder, T.-L. Lee, L. Libralesso, I. Joumard, J. Zegenhagen, P. Zaumseil, C. Wenger, G. Lupina, G. Lippert, J. Dabrowski, and H.-J. Müssig. Structure and strain relaxation mechanisms of ultrathin epitaxial Pr_2O_3 films on Si(111). *J. Appl. Phys.*, 97(7):074906, 2005. `doi:10.1063/1.1883304`.

[32] T. Schroeder, P. Zaumseil, G. Weidner, G. Lupina, Ch. Wenger, H.-J. Müssig, and P. Storck. Structure, twinning behavior, and interface composition of epitaxial Si(111) films on hex-Pr_2O_3(0001)/Si(111) support systems. *J. Appl. Phys.*, 98(12):123513, 2005. `doi:10.1063/1.2149186`.

[33] T. Schroeder, P. Zaumseil, G. Weidner, Ch. Wenger, J. Dabrowski, H.-J. Müssig, and P. Storck. On the epitaxy of twin-free cubic (111) praseodymium sesquioxide films on Si(111). *J. Appl. Phys.*, 99(1):014101, 2006. `doi:10.1063/1.2136788`.

[34] G. Lupina, T. Schroeder, J. Dabrowski, Ch. Wenger, A. U. Mane, H.-J. Müssig, P. Hoffmann, and D. Schmeisser. Praseodymium silicate films on Si(100) for gate dielectric applications: Physical and electrical characterization. *J. Appl. Phys.*, 99(11):114109, 2006. `doi:10.1063/1.2202235`.

[35] W. Pies and A. Weiss. *Landolt-Börnstein - Group III Condensed Matter Numerical Data and Functional Relationships in Science and Technology. In: Crystal Structure Data of Inorganic Compounds.* Springer, 1975.

[36] X-Ray Interactions With Matter Database. `http://henke.lbl.gov/optical_constants/getdb2.html`, 30.10.2007.

[37] N. M. Jeutter. Wachstum von Praseodymoxid auf Silizium (111) und (113), 2005. PhD thesis. Available from: `http://www.lrz-muenchen.de/~surfacescience/Talks/Thesis.pdf`.

[38] A. Schaefer. Struktur und Wachstum von dünnen Praseodymoxidschichten auf Silicium-Substraten, 2006. Diplomarbeit.

[39] Thin Film Evaporation - Common Materials Reference and Guide. `http://ee.byu.edu/cleanroom/TFE_materials.phtml`, 17.06.2009.

[40] E. Fendt. Strukturuntersuchungen an dünnen Flüssigkeitsfilmen, 2003. Diplomarbeit.

[41] T. Weisemoeller, C. Deiter, F. Bertram, S. Gevers, A. Giussani, P. Zaumseil, T. Schroeder, and J. Wollschlaeger. Epitaxy of single crystalline PrO_2 films on Si(111). *Appl. Phys. Lett.*, 93(3), 2008. `doi:10.1063/1.2958227`.

[42] T. Weisemoeller, F. Bertram, S. Gevers, A. Greuling, C. Deiter, H. Tobergte, M. Neumann, J. Wollschläger, A. Giussani, and T. Schroeder. Postdeposition annealing induced transition from hexagonal Pr_2O_3 to cubic PrO_2 films on Si(111). *J. Appl. Phys.*, 105(12):124108, 2009. `doi:10.1063/1.3152796`.

[43] T. Weisemoeller, F. Bertram, S. Gevers, C. Deiter, A. Greuling, and J. Wollschläger. Effect of amorphous interface layers on crystalline thin-film x-ray diffraction. *Phys. Rev. B*, 79(24):245422, 2009. `doi:10.1103/PhysRevB.79.245422`.

[44] S. Hahne. Strukturanalyse von Praseodymoxidschichten mit Röntgenbeugung, 2008. Bachelor thesis.

[45] S. Gevers, T. Weisemoeller, B. Zimmermann, F. Bertram, C. Deiter, and J. Wollschlaeger. Structural phase transition of ultra thin PrO_2 films on Si(111). *J. Phys.: Condens. Matter*, 21(17), 2009. `doi:10.1088/0953-8984/21/17/175408`.

[46] C Boulesteix and L Eyring. Reduction of praseodymium and terbium higher oxides: Chemical reactions similar to diffusionless phase transitions. 71(2):458, 1987. `doi:10.1016/0022-4596(87)90255-6`.

[47] A.T. Lowe, K.H. Lau, and L. Eyring. The effect of crystal size on chemical hysteresis in praseodymium and terbium oxides. *J. Solid State Chem.*, 15(1):9, 1975. `doi:10.1016/0022-4596(75)90265-0`.

[48] J.M. Haschke and L. Eyring. Hydrothermal equilibriums and crystal growth of rare earth oxides, hydroxides, hydroxynitrates, and hydroxycarbonates. *Inorg. Chem.*, 10(10):2267, 1971.

[49] Z.C. Kang and L. Eyring. The solvolytic disproportionation of mixed-valence compounds: II. $Tb_{11}O_{20}$. *J. Solid State Chem.*, 75(1):60, 1988. `doi:10.1016/0022-4596(88)90303-9`.

[50] J.P. Liu, P. Zaumseil, E. Bugiel, and H.J. Osten. Epitaxial growth of Pr_2O_3 on Si(111) and the observation of a hexagonal to cubic phase transition during postgrowth N_2 annealing. *Appl. Phys. Lett.*, 79:671, 2001. `doi:10.1063/1.1389509`.

[51] P. Zaumseil. X-ray measurement of the tetragonal distortion of the oxide buffer layer in Ge/Pr_2O_3/Si(111) heteroepitaxial structures. *J. Phys. D: Appl. Phys.*, 41(13), 2008. `doi:10.1088/0022-3727/41/13/135308`.

[52] Rhéal P. Turcotte, Joyce M. Warmkessel, Richard J. D. Tilley, and Leroy Eyring. On the phase interval $PrO_{1.50}$ to $PrO_{1.71}$ in the praseodymium oxide-oxygen system. *J. Solid State Chem.*, 3(2):265, 1971. `doi:10.1016/0022-4596(71)90039-9`.

[53] B. G. Hyde, E. E. Garver, U. E. Kuntz, and L. Eyring. Kinetic Studies on Reactions of Praseodymium Oxides in an Oxygen Atmosphere: $PrO_{1.83} + O_2 \rightleftharpoons PrO_2$. *J. Phys. Chem.*, 69(5):1667, 1965. `doi:10.1021/j100889a037`.

[54] J. B. MacChesney, H. J. Williams, R. C. Sherwood, and J. F. Potter. Concerning the magnetic susceptibility of praseodymium oxides. *The Journal of Chemical Physics*, 41(10):3177, 1964. `doi:10.1063/1.1725693`.

[55] E. Summerville, R. Tuenge, and L. Eyring. High-resolution crystal structure images of beta phase $Pr_{24}O_{44}$ in the praseodymium oxide system. *J. Solid State Chem.*, 24(1):21, 1978. `doi:10.1016/S0022-4596(78)90180-9`.

List of Figures

2.1 Coolidge tube, image taken from [7]. Voltage U_h is applied to the filament, which is in consequence heated so that electrons are emitted. These are accelerated by voltage U_a and decelerated when they hit the anode A. Due to this deceleration, X-rays X are emitted. The anode is cooled by the water cooler C with water connections W$_{out}$ and W$_{in}$. 3

2.2 Atom model for X-ray emission in a tube, image taken from [8] and modified. External stimulation causes electrons to be emitted, the resulting electron holes are filled by electrons from higher shells. Excess energy is emitted in the form of X-radiation and contributes the characteristic part of the radiation. 4

2.3 Brilliance with time, image taken from [9]. The development of synchrotron radiation sources enhanced the peak brilliance of X-ray sources dramatically. Free electron lasers provided further improvement recently. 5

2.4 Sketch of an undulator/wiggler, image taken from [10]. Periodically ordered dipole magnets force the traversing particle beam to oscillate and radiate. . . 6

2.5 X-ray reflection and refraction at an interface. An X-ray beam hits the interface under an incidence angle α_i and is partly reflected under an angle $\alpha_f = \alpha_i$. The remaining part of the beam is refracted and transmitted under an angle α_t. In contrast to conventional optics, where angles are measured between direction of propagation and *surface normal*, the angles are measured between direction of propagation and *surface* in X-ray reflection. 7

2.6 Simulated intensity of a wave reflected at a vacuum/Si interface. The photon energy is 10 keV and an intensity R of 1.0 means that the wave is totally reflected. The simulation includes a linear increase of the reflected intensity with small scattering vectors. This *footprint* is due to the assumed finite size of the sample and the three-dimensional extension of the beam. 9

2.7 X-ray reflectivity at multiple interfaces, image taken from [11] and translated. A part of the previously transmitted beam T_{j-1} (red) is reflected at the interface at z_{j-1} as beam R_{j-1} (blue), the rest of the beam is transmitted as T_j. The distance between two interfaces is d_j. Multiple scattering effects are taken into account, so that a part of the reflected wave R_j is reflected again at the interface at z_{j-1}. Its amplitude is therefore added to T_j. 10

2.8 Simulated intensity of a wave reflected at a substrate with 10 nm praseodymium dioxide on top. The photon energy is 10 keV and an intensity R of 1.0 means that the wave is totally reflected. Interfaces are perfectly sharp (no roughness). The angle dependent oscillations are due to the oxide layer of finite thickness. 12

2.9 Bragg condition using the example of X-ray reflectivity, image taken from [14] and modified. The path difference (dark red) between the waves (blue) reflected at the under and upper layer (black) is $\delta = 2d \sin\Theta$ with the distance between the layers d and the incidence angle Θ. If this incidence angle dependent path difference is a multiple of the wavelength, constructive interference occurs. . . 13

2.10 Bragg condition at atomic planes, image taken from [17]. Waves diffracted at periodically ordered layers with distance d have a path difference of $2a = 2d \sin \vartheta$. If this path difference is a multiple of the wavelength for neighboring layers, the same is also true for the path difference between any equidistant layers. The Bragg condition is fulfilled and waves diffracted at all these layers therefore interfere constructively for certain scattering vectors. 15

2.11 N-slit function for $N = 6$, image taken from [19]. $N - 2$ fringes occur between the main maxima at $x = 0$ and $x = 2\pi$. These are typical of diffraction patterns originating from one-dimensional periodically ordered scattering centers. . . . 19

2.12 Diffraction at different crystal structures, image taken from [20] and revised. The intensity distribution of a wave diffracted at a *bulk* crystal gives high intensity only at the (zero-dimensional) Bragg spots. A two-dimensional surface (*2D layer*) gives an only two-dimensional Bragg condition, so that the diffracted intensity has a one-dimensional distribution. A two-dimensional surface on an infinite bulk crystal gives a combination of the two diffraction patterns. A semi-infinite crystal causes Bragg spots that are not perfectly sharp perpendicular to the surface. The resulting diffraction patterns are called *Crystal Truncation Rods* (CTRs). 20

2.13 Surface roughness of a semi-infinite crystal, image taken from [19]. Different layer numbers N_3 at different lateral coordinates (n_1, n_2) describe the surface roughness. 21

2.14 Roughness of a (ultra-)thin layer, image taken from [19]. The roughnesses at top and bottom is calculated assuming standard deviation of the film expansion in top direction $N_3^+(n_1, n_2)$ and bottom direction $N_3^-(n_1, n_2)$. 23

2.15 Schematic drawing of a crystalline system. Each layer m consists of a number of unit cells, which are shifted by $\boldsymbol{j_m}$, respectively. The bottom unit cell of a layer j is shifted from the topmost unit cell of the subjacent layer by $\boldsymbol{g_m}$. . . 24

2.16 Scheme of X-ray photoelectron spectroscopy, image taken from [22]. A photon hits a core electron and transfers its energy to this electron. Part of the former photon energy is used to overcome the binding energy, the rest of the energy becomes the kinetic energy of the now free electron. 26

2.17 Si unit cell, image taken from [24]. Two face-centered unit cells, separated by 1/4 of the unit cell width in each dimension, form the diamond structure. . . 28

2.18 Unit cells of (from left to right) c-PrO_2, h-Pr_2O_3 and c-Pr_2O_3, image taken from [28]. The latter is basically identical to c-PrO_2, but has periodically ordered oxygen vacancies. Praseodymium atoms are shown in black color, oxygen atoms in red color. 29

2.19 Partial phase diagram of *bulk* praseodymium oxide, image taken from [28]. Illustrated are the equilibrium stoichiometries, which depend on temperature and oxygen ambient pressure. 30

2.20 Simulated XRR data for PrO_2 (black line) and c-Pr_2O_3 (red line), assuming photon energies of 10 keV. The differences due to the different indices of refraction are very small. 32

3.1 UHV chamber at the IHP in Frankfurt (Oder). The actual evaporation of praseodymium oxide takes place in the chamber at the lower right. 33

3.2 Furnace for post deposition annealing of the samples in oxygen. Temperatures were varied from sample to sample and the annealing time was 30 minutes. . 35

3.3 Six circle diffractometer, image taken from [40] and edited. The primary beam is damped by the absorber and reduced in size by slits, its intensity is controlled by the monitor. The beam is reflected/diffracted by the sample and the detector measures the intensity at a given position. During the XRR and XRD measurements, only incidence angle *om* and detector angle *tt* are moved. The remaining motors, indicated by the bent arrows, are only moved slightly and only during the alignment of the sample. 36

3.4 Miscut of a crystalline sample. The surface for XRR along the topmost atoms of the sample (blue line) differs slightly from the surface for XRD along the crystal planes (red line). The difference between these two directions Δ *om* is also called the *miscut* and is $(0.35 \pm 0.15)^\circ$ for the substrates used in this work. 37

3.5 *RodsNPlots* screenshot. The top right area defines the model, the top left area sets the fitting algorithm. At the bottom, measured data (black dots) is compared to the calculated intensity distribution (red line) according to the model above. The individual intensity contributions of the two columns is shown by the green lines, respectively. 38

3.6 *iXRR* screenshot. The top right area defines the model, the top left area sets the fitting algorithm. At the bottom, measured data (red dots) is compared to the calculated intensity distribution (blue line) according to the model above. 39

7.1 Simulation of a PrO_2 substrate with an oxygen atom missing in every second unit cell(vertically) and without roughness (blue dash-dotted line). Compared to PrO_2 without oxygen vacancies, additional Bragg peaks at $L = \frac{2N+1}{2}$ with $N \in \mathbb{N}$ occur due to the larger unit cell. A *non doubled* PrO_2 unit cell (black line) correctly shows the same intensity distribution as the *doubled* PrO_2 unit cell (red dashed line). Reciprocal lattice units (r.l.u.) are chosen with respect to the *non* doubled PrO_2 unit cell. 48

7.2 Simulation of different PrO_2 substrates *with* surface roughness. The substrate consisting of single PrO_2 unit cells (black line) is calculated correctly. The substrates of doubled PrO_2 unit cells *with* oxygen vacancies (blue dash-dotted line) and *without* (red dashed line) oxygen vacancies incorrectly show a broad peak at $L = \frac{2N+1}{2}$ with $N \in \mathbb{N}$. Comparison with the PrO_2 substrate without roughness (dashed green line, identical to the black line from Fig. 7.1) confirms that at $L = \frac{2N+1}{2}$ with $N \in \mathbb{N}$, damping shows no effect for the doubled unit cells. Furthermore, the blue dash-dotted line for the substrate with oxygen vacancies correctly shows peaks at $L = \frac{2N+1}{2}$ with $N \in \mathbb{N}$ due to the oxygen superstructure. 49

7.3 Pressure temperature relations for the higher praseodymium oxides, data taken from [54]. Depending on temperature and oxygen partial pressure, the equilibrium stoichiometry is either PrO_2 (upper left of the black dividing line) or Pr_6O_{11} (lower right of the black dividing line). The blue dashed line marks the pressure used for post deposition annealing of the samples prepared in the context of this thesis. The red dash-dotted line marks the partial pressure of air. It is important to note that these are *equilibrium* stoichiometries. The (de-)oxidation process slows down significantly at lower temperatures. 55

B Acknowledgment

I would like to thank many people that supported me in the preparation of this thesis.

Second to none, this is my thesis advisor Prof. Dr. Joachim Wollschläger, who proved himself not only knowledgeable, but also remarkably patient and open-minded. These are the qualities that made working in our newly formed group so enjoyable and also productive. I guess that we would have missed the most important results in a different working atmosphere.

Prof. Prof.h.c. Dr. Dr.h.c. Manfred Neumann filled the role of the secondary advisor regardless of time constraints. Thank you for that, and for the fruitful discussions about the stubborn praseodymium oxide system and XPS.

I would also like to thank our cooperative partners from IHP, namely Dr. Thomas Schroeder, Alessandro Giussani, Dr. Olaf Seifarth and Dr. Peter Zaumseil.

Furthermore, I want to highlight the direct support of my work by various members of our group. Naming all of them would here would break the mould, but Sebastian Gevers, Florian Bertram, Andreas Greuling, Dr. Carsten Deiter and Susanne Hahne should surely be mentioned.

Special thanks go to my dear office colleagues Gregor Steinhoff, Bernd Zimmermann and Oliver Höfert, who endured the wicked atmosphere all the time and became good friends of mine.

Last but not least I want to thank my friends and family. Betty, you are the most important person for me and make my life an extremity of joy. Mom, dad, my dear brother, I know that the trust and goodwill you give to me is not a matter of course, and I owe my happiness and strength to you.

The same is true for the support of my potential parents-in-law, Margret and Heinz-Georg, and for my best friends Michael Schiffbänker and Oliver Störmann.

Thank you all for the great time I had while I worked on this thesis.